

2-18
7/17

NASA CR 130183

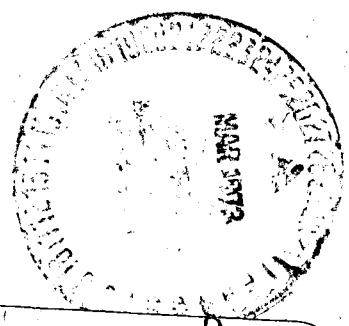
STAR

OPTICAL TO OPTICAL INTERFACE DEVICE

Donald S. Oliver, Paul Vohl, and Peter Nisenson
Itek Corporation
Central Research Laboratories
10 Maguire Road
Lexington, Massachusetts 02173

November, 1972
Final Project Report

Prepared for
GODDARD SPACE FLIGHT CENTER
Greenbelt, Maryland 20771



(NASA-CR-130183) OPTICAL TO OPTICAL
INTERFACE DEVICE Final Project Report, N73-19671
Jun. 1971 - Feb. 1972 (Itek Corp.)
83 p HC \$6.25
CSCL 20F
G3/23 Unclas
65525

OPTICAL TO OPTICAL INTERFACE DEVICE

Donald S. Oliver, Paul Vohl, and Peter Nisenson
Itek Corporation
Central Research Laboratories
10 Maguire Road
Lexington, Massachusetts 02173

November, 1972
Final Project Report

Prepared for
GODDARD SPACE FLIGHT CENTER
Greenbelt, Maryland 20771

1. Report No.	2. Gov. Accession No.	3. Recipient's Catalog No.
4. Title and Subtitle OPTICAL TO OPTICAL INTERFACE DEVICE		5. Report Date November, 1972
7. Authors D. S. Oliver, P. Vohl, and P. Nisenson		6. Performing Org. Code
9. Performing Organization Name and Address Itek Corp., Central Research Laboratories 10 Maguire Road Lexington, Massachusetts 02173		8. Performing Org. Report No. Project 9655
12. Sponsoring Agency Name and Address James Strong, III Goddard Space Flight Center Greenbelt, Maryland 20771		10. Work Unit No.
15. Supplementary Notes		11. Contract or Grant No. NAS 5-11486
		13. Type of Report and Period Covered Final Project Report June 1971- Feb. 1972
		14. Sponsoring Agency Code
16. Abstract A project to fabricate, demonstrate, and deliver a real time incoherent to coherent optical converter having applications in real-time coherent optical processing systems was undertaken. The device utilizes the natural photo-conductivity effect to spatially modulate the electrical polarization in the single crystalline electro-optic material, $\text{Bi}_{12}\text{SiO}_{20}$. An optically absorbed write-in image is stored as an image-wise polarization pattern in the device. Readout is accomplished electro-optically by means of the subsequent phase retardation which a polarized beam of coherent light undergoes in passing through the $\text{Bi}_{12}\text{SiO}_{20}$. An advantage of this device is the unique way in which the photoconductive effect is combined with the electro-optic effect in a single active material. An operating mode for achieving continuous image conversion with high speed recyclability is utilized. The following characteristics have been demonstrated: A write-in intensity of $300 \mu\text{-watts/cm}^2$ at 400 nm yielded a contrast ratio of 50:1 after 40 milliseconds exposure. When the converter was operated at a frame rate of 10 per second, a sampled readout contrast ratio of greater than 1,000:1 was achieved. Resolution in excess of 80 lp/mm has been recorded and readout. The crystal growing and device fabrication methods by which 1 square inch converters have been built and operated are described and results achieved in using this device to Fourier transform images are presented.		
17. Key Words Incoherent to coherent converter -Real time optical processing - electro-optic modulator		18. Distribution Statement
19. Security Classif. (of this report) Unclassified		20. Security Classif. (of this page) Unclassified
21. No. of Pages 85		22. Price 6.25



PREFACE

The objective of this project was to develop, fabricate, and deliver two real time incoherent to coherent optical interface devices and associated drive electronics. The devices were to be capable of converting incoherent optical images into coherent light patterns which could undergo a subsequent Fourier transform filtering operation and inverse transformation to produce a filtered coherent image.

The design approach utilized the natural photoconductivity effect to spatially modulate the electrical polarization in the single crystalline electro-optic material, $\text{Bi}_{12}\text{SiO}_{20}$. An optically absorbed write-in image is stored as an image-wise polarization pattern in the device. Readout is accomplished electro-optically by means of the subsequent phase retardation which a polarized beam of coherent light undergoes in passing through the $\text{Bi}_{12}\text{SiO}_{20}$. An operating mode for achieving continuous image conversion with high speed recyclability is utilized. The scope of the work included the growth of $\text{Bi}_{12}\text{SiO}_{20}$ along with the fabrication of devices from polished crystal slices.

Two devices were delivered to NASA Goddard during the course of this project and performed in accordance with the work statement. Measurements indicated a write-in intensity of 300 microwatts/cm² at 400 nm would yield a contrast ratio of 50:1 after 40 milliseconds exposure. When the converter was operated at a frame rate of 10 per second, a sampled readout contrast ratio of greater than 1000:1 was achieved. Resolution in excess of 80 lp/mm has been recorded and readout. Photographic results achieved in using this device to Fourier transform images are presented in Figures 6-6 through 6-12.

It is proposed that the current device be combined with an image intensifier (utilizing fiber optic coupling) to produce an improved structure in terms of spectral sensitivity and logical (parallel processing) flexibility.

Preface - Continued

Although an improved structure is proposed existing devices should be fully characterized as to photosensitivity, stability of operation, modulation transfer function, and response time to guide further materials and device improvement work.

CONTENTS

Preface	iii
Contents	v
Illustrations	vii
Tables	ix
1. Introduction	1
2. Theory of PROM Operation and Its Application as an Incoherent to Coherent Converter	
2.1 History of PROM	1
2.2 PROM Device Structure	2
2.3 PROM Theory of Operation	4
2.4 Framing Mode of Operation	8
2.5 Optimum Device Geometry for a Noncoherent to Coherent Converter	12
3. Growth of Bi ₁₂ SiO ₂₀ Crystals	13
3.1 Procedure	13
3.2 Crystal Strain	18
4. Device Fabrication and Evaluation	
4.1 Slicing and Polishing	24
4.2 Electrical and Optical Evaluation of Wafers	24
4.3 Dichroic Reflector	24
4.4 Parylene Coatings	26
4.5 Completion of the Device	26
4.6 Device Evaluation Techniques	26
4.7 Contrast Ratio	30
4.8 Sensitivity	30
4.9 Additional Measurements	33
5. Electronic Drive Equipment	
5.1 Programmable Power Supply	34
5.2 Pulse Generator	34
5.3 Xenon Flashlamp and Power Supply	36

Contents - Continued

6.	Performance Tests	
6.1	System Requirements	37
6.2	Optical Apparatus	37
6.3	Initial Filtering Experiments	41
6.4	Converter Operational Characteristics	44
6.5	Photographic Results	46
7.	Problems Encountered	
7.1	Crystal Cracking	54
7.2	Birefringent Strain	54
7.3	Contrast Ratio	54
7.4	Sensitivity	55
7.5	Strain	55
7.6	Reflections and Coherent Interference Patterns	55
8.	Project Results	57
9.	Recommendations	58
10.	New Technology	61
11.	Appendixes	
11.1	Diffraction Efficiency Calculations	62
11.2	Quantum Efficiency Calculation	70
12.	References	72

ILLUSTRATIONS

2-1	Photosensitive Pockels effect light valves	3
2-2	Pockels effect in a cubic crystal	5
2-3	Operation of PROM	7
2-4	Spectral sensitivity of ZnS, ZnSe, and $\text{Bi}_{12}\text{SiO}_{20}$	8
2-5	Analyzer outputs for high contrast inputs	11
3-1	Apparatus for growing electro-optic material	14
3-2	Laue pattern of $\text{Bi}_{12}\text{SiO}_{20}$ crystal	15
3-3	As grown $\text{Bi}_{12}\text{SiO}_{20}$ crystal	17
3-4	Polished and etched wafers	21
3-5	Etch patterns in $\text{Bi}_{12}\text{SiO}_{20}$	22
3-6	Etch patterns in $\text{Bi}_{12}\text{SiO}_{20}$	23
4-1	Optical to optical interface device	25
4-2	Parylene deposition apparatus	27
4-3	Electron diffraction pattern for Parylene	28
4-4	Experimental setup for device evaluation	29
4-5	Experimental discharge trace	31
4-6	Absorption coefficient and spectral sensitivity of device	32
5-1	Electronic drive schematic for optical interface device	35
6-1	Optical apparatus for performance testing OID (transparent targets)	38
6-2	Optical apparatus for performance testing OID (reflective targets)	39
6-3	OID output image of 10 lp/mm crossed grating	42
6-4	Power spectra of 10 lp/mm (grating as seen in Fourier plane)	45
6-5	Grating with one set of lines removed by inserting slit filter in Fourier plane located between OID and output plane	45
6-6	OID output images using three-bar single frequency input target	50
6-7	OID output images using multi-bar multi-frequency input target	50
6-8	OID output images using triangle target	51
6-9	OID output images using checkerboard target (transmitting)	51
6-10	OID output images using airstrip target	52
6-11	OID output images using checkerboard target (reflecting)	52
6-12	OID output image for low frequency target (reflecting) plus strain pattern and no signal pattern	53
9-1	Proposed incoherent to coherent image converter tube	60

A-1	First-order diffraction efficiency (crossed analyzer)	65
A-2	First-order diffraction efficiency ($\phi_A = \pi/2$)	66
A-3	First-order diffraction efficiency ($\phi_A = \pi/3$)	67
A-4	First-order diffraction efficiency ($\phi_A = \pi/4$)	68
A-5	First-order diffraction efficiency ($m = 1$)	69

TABLES

3-1	Spectrographic Analysis of $\text{Bi}_{12}\text{SiO}_{20}$	18
5-1	Pulse Generator Logic Module Specifications	36
6-1	Description of Performance Test Targets and Output Image Photographs	48

1. INTRODUCTION

This project was concerned with the development, fabrication, and testing of a preliminary model of an optical-to-optical (noncoherent-to-coherent) interface device for use in coherent optical parallel processing systems. The developed device demonstrates a capability for accepting as an input a scene illuminated by a noncoherent radiation source and providing as an output a coherent light beam spatially modulated to represent the original noncoherent scene.

The converter device developed under this contract employs an Itek Pockels readout optical modulator (PROM). This is a photosensitive electro-optic element which can sense and electrostatically store optical images. The stored images can be simultaneously or subsequently readout optically by utilizing the electrostatic storage pattern to control an electro-optic light modulating property of the PROM. The readout process is parallel since no type of scanning mechanism is required.

The PROM unlike other light image controlled modulators provides the functions of optical image sensing, modulation, and storage in a single active material. During the course of this contract crystals of this electro-optic material (bismuth silicon oxide) were grown, sliced and polished and the finished slices were used to fabricate PROM devices. Subsequently these devices were evaluated as noncoherent-to-coherent converters by exposing them to image patterns of noncoherent radiation and measuring the definition, contrast, and intensity of the imagewise modulated coherent readout radiation in both the Fourier transform and image planes of the readout optical system.

2. THEORY OF PROM OPERATION AND ITS APPLICATION AS AN INCOHERENT TO COHERENT CONVERTER

2.1 History of PROM -

Itek has conducted an in-house research and development program concerned with reusable optical image storage and processing devices since 1967. The semiconductor material used in these devices photoconductively

converts and electrostatically stores optical images which can be optically read out using the Pockels electro-optic effect generated in the material by the electrostatic image. Write-in and readout can take place simultaneously and at different electromagnetic wavelengths, thus forming the basis for a real-time noncoherent-to-coherent converter.

Initial public disclosures[1]-[2] were made on a long term storage device using epitaxial films of ZnS as the photosensitive electro-optic material. Subsequently PROM devices have been fabricated using bismuth silicon oxide ($\text{Bi}_{12}\text{SiO}_{20}$) [3] which is electro-optically superior to ZnS, having a Pockels effect approaching that of DKDP. Furthermore, the material is easily grown by the Czochralski method and crystals providing useful areas over 1 cm^2 had been grown prior to this contract. The electrical and optical properties and growth techniques for these photoconductive electro-optic materials have been reported in the literature [4]-[9].

2.2 PROM Device Structure -

Figure 2-1 shows the two basic device structures which have been fabricated and tested. Figure 2-1(a) depicts the configuration used when the active material is a single crystal of ZnSe or $\text{Bi}_{12}\text{SiO}_{20}$. The Parylene¹ insulating layers and transparent Pt electrodes are evaporated films applied to the polished crystal surfaces. The operation of this type of device as an optical memory having image reversing (e.g. positive-to-negative) and selective update features has been described in the literature [3] and its theory of operation is reviewed below.

The device configuration shown in Figure 2-1(b) is employed when the active material is an epitaxial layer of ZnS (or ZnSe) grown on a GaAs substrate. This type of device has also been reported in the literature [1], [2] as a high resolution (85 lp/mm) image sensing (100 ergs/cm^2 exposure) and memory (100 hour dark storage) device capable of storing gray scale images with high fidelity.

1. Class of p-xylylene polymers manufactured by the Union Carbide Corp.

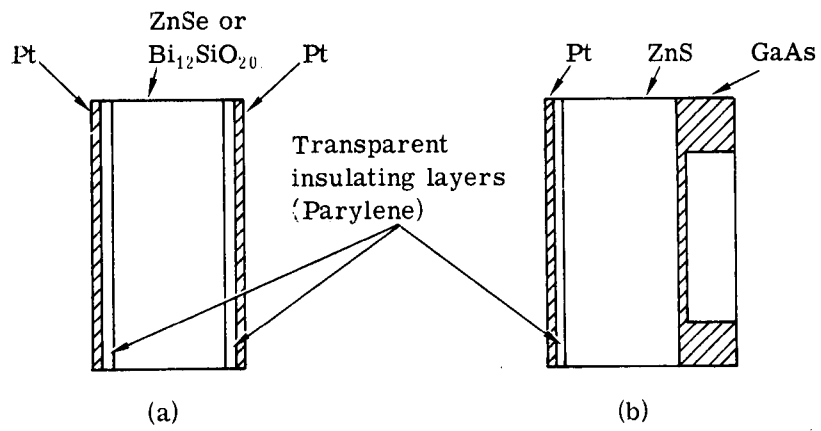


Fig. 2-1 Photosensitive Pockels effect light valves

Both devices shown are read out in transmission. The ZnS/GaAs device is read out in transmission by selectively etching a window into the GaAs substrate to provide a thin transparent electrode at the ZnS/GaAs interface. Reflective readout, which affords a double pass through the electro-optic layer, has also been accomplished utilizing reflected light from the ZnS/GaAs interface. The configuration shown in Fig. 2-1(a) can be made into a reflective readout device by depositing a multilayer dichroic reflector onto one of the electro-optic crystal surfaces prior to evaporating the Parylene layer. The reflector is designed to transmit the short write-in wavelengths and reflect the long readout wavelengths.

2.3 PROM Theory Of Operation -

The principle of readout operation in the PROM is the Pockel's effect in the electro-optic crystal as illustrated in Figure 2-2. A voltage applied between the (100) faces of a cubic electro-optic crystal causes it to become birefringent, i. e., light polarized along one axis (F) travels faster than light polarized along a perpendicular axis (S). If the readout light is plane polarized and oriented to bisect the birefringent axes, then the light leaving the crystal will be elliptically polarized with major and minor axis intensity components as shown. Thus, an analyzer crossed 90 degrees to the initial polarization of the light will transmit an intensity component of magnitude $I_1 \sin^2 KV$; where V is the voltage drop across the crystal.

An image may be impressed on this readout light beam by spatially varying the magnitude of voltage across the crystal in an imagewise pattern. This is accomplished by utilizing the photoconductivity inherent in the crystal. Once the crystal is charged to a given voltage, the voltage can be imagewise decayed by a write-in light image that is absorbed by the crystal, generating carriers in the light-struck areas. These photo generated carriers move in the electric field in a direction to neutralize the external charges thereby reducing the crystal voltage towards zero.

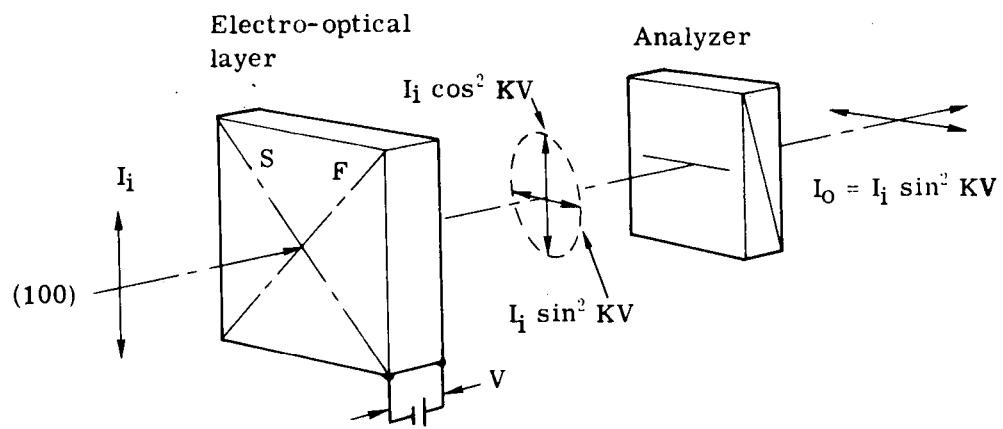


Fig. 2-2 Pockels effect in a cubic crystal

In practice the write/read operations are carried out as shown in Figure 2-3. Initially, there is an erase and prime operation as shown by operations (a), (b), and (c). In operation (a), a bias voltage is applied across the insulating layers and crystal. The heavy line through the structure illustrates the relative voltage at each point in the structure. In operation (b), uniform illumination by a xenon flash of a few microseconds duration generates positive and negative charge carriers that move in the electric field to the interfaces between the crystal and the blocking insulators, where they are trapped. The field due to these trapped charges exactly cancels the applied field from the battery voltage across the electrodes, so that the voltage across the crystal becomes zero. The applied voltage thus appears only across the insulating layers. Note that this operation also serves to erase previously stored images. In operation (c), the applied voltage is removed, and the electrodes are shorted together. As a result, the field in the crystal due to the trapped charge is no longer compensated by the field from the applied voltage. A uniform voltage now appears across the crystal approximately equal to the original bias voltage.

The device is now ready for image write-in shown in operation (d). The top half illustrates an exposed area of the crystal, and the bottom half an unexposed area. The voltage remains high in the unexposed area. In the exposed area, separation of the photogenerated carriers reduces the electro-optical voltage in the crystal. In operation (e) reflective readout is shown using polarized red light, to which the material is only slightly photosensitive. Where the voltage is high, the electro-optical effect creates elliptical polarization, increasing the readout light passed by the analyzer. In the areas where the voltage is decayed, the readout remains linearly polarized and does not pass through the analyzer. A negative of the write-in image is thus produced.

At this point, if the battery voltage is reapplied, the field produced will act in the opposite direction to the existing imagewise fields in the

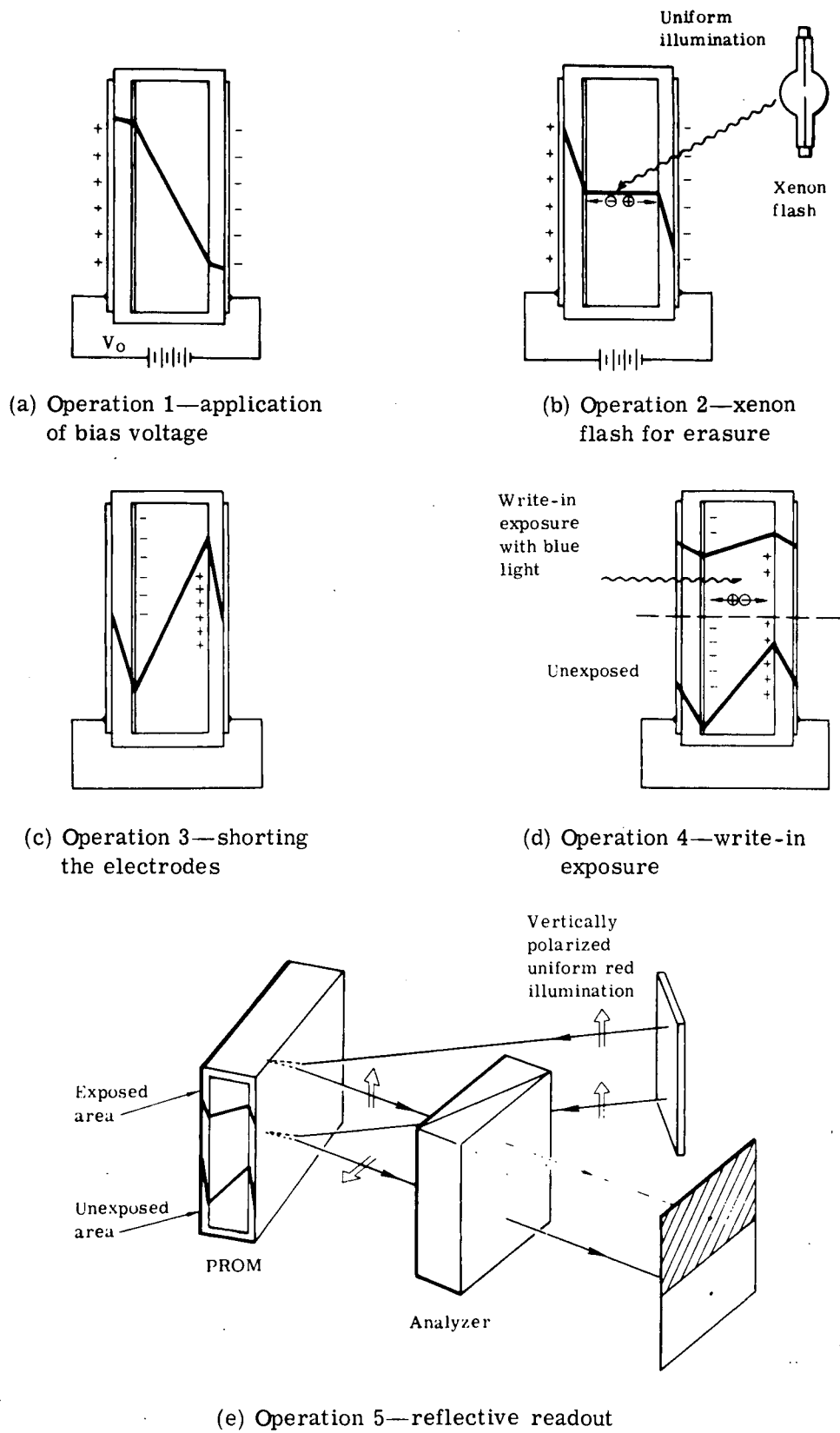


Fig. 2-3 Operation of PROM

crystal. Thus, the high field regions will be reduced to zero and the low field regions will be raised to the biasing field. The new voltage pattern is therefore the reverse of the original imagewise pattern and the image read out is thus electrically reversed from a negative to a positive image.

The strongly wavelength-dependent nature of the crystal's photosensitivity plays an essential part in the operation of the device. The spectral sensitivity of the materials used (see Figure 2-4) shows a pronounced peak in the blue region of the visible spectrum and falls rapidly toward the red and the near infrared. One indeed capitalizes on the large difference in the input photosensitivities between blue and red by writing an image in the blue and reading out in the red or infrared. A stored image can be readout with an intensity gain, without an appreciable degradation of image contrast. This permits the flexibility of two different readout modes: many high intensity short pulses, or a low intensity continuous wave readout over a long period of time. It should be noted that any combination of coherent or incoherent light sources may be used for write-in and readout. This makes the device usable in either incoherent or coherent processing systems or as an incoherent to coherent optical converter.

In addition to optical to optical conversion accomplished by using the photoconductive and electro-optical effects of the crystal, there is an image storage effect that occurs after the write-in light image is turned off. This storage occurs because the electro-optic crystal has extremely high dark resistance so that any voltage pattern impressed on the crystal will not decay for several hours. This allows the image to be readout at a later time.

2.4 Framing Mode Of Operation -

When considering the use of the PROM as a real time noncoherent-to-coherent converter it must be remembered that the above mentioned storage effect causes the device to act as an integrating photosensor analogous to photographic film. Therefore, like photographic film it is preferable to operate the device in a framing mode when

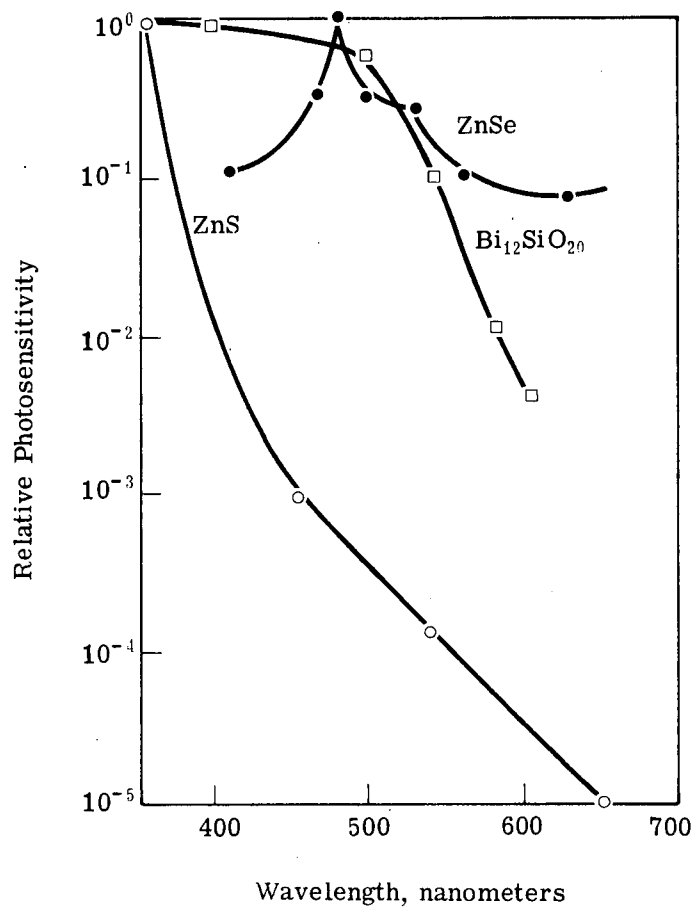


Fig. 2-4 Spectral sensitivity of ZnS, ZnSe, and Bi₁₂SiO₂₀

the input imagery is changing with time. The erase and prime operation described above is therefore repeated at a rate dictated by the desired coherent image generation time. In this project the design objective was to have the converter reach its steady state condition within 100 milliseconds after the introduction of a new image. Furthermore an output image intensity contrast ratio of 50X was desired when the converter was exposed to high contrast noncoherent input imagery.

Figure 2-5 shows the analyzer output light intensity as a function of time when the PROM is continuously exposed to a high contrast input image and a 5 millisecond erase/prime operation is repeated every 100 milliseconds. The top graph is the coherent output in a region where the input light is a minimum and the bottom graph in a region where the input light is a maximum. If the output light is viewed continuously then the ratio of average intensities determines the contrast.

The average intensity of the top graph is given by:

$$0.05 (0) + 0.95 I, \quad (1)$$

where I is the peak analyzer output intensity. The average intensity of the bottom graph is given by:

$$I \left[0.05 (t_1)^{-1} \int_0^{t_1} \exp[-t/\tau_1] dt + 0.95 (t_2)^{-1} \int_0^{t_2} \exp[-t/\tau_2] dt \right], \quad (2)$$

Where t_1 and t_2 are 5 and 95 milliseconds respectively.

Expression (2) reduces to:

$$0.05 I \tau_1 t_1^{-1} + 0.95 I \tau_2 t_2^{-1}, \quad (3)$$

if τ_1 and τ_2 are much smaller than t_1 and t_2 respectively. Therefore, the average contrast becomes equal to the ratio of expression (1) to (3) or:

$$t_2 \tau_2^{-1}, \quad (4)$$

again assuming that τ_1 is much smaller than t_1 .

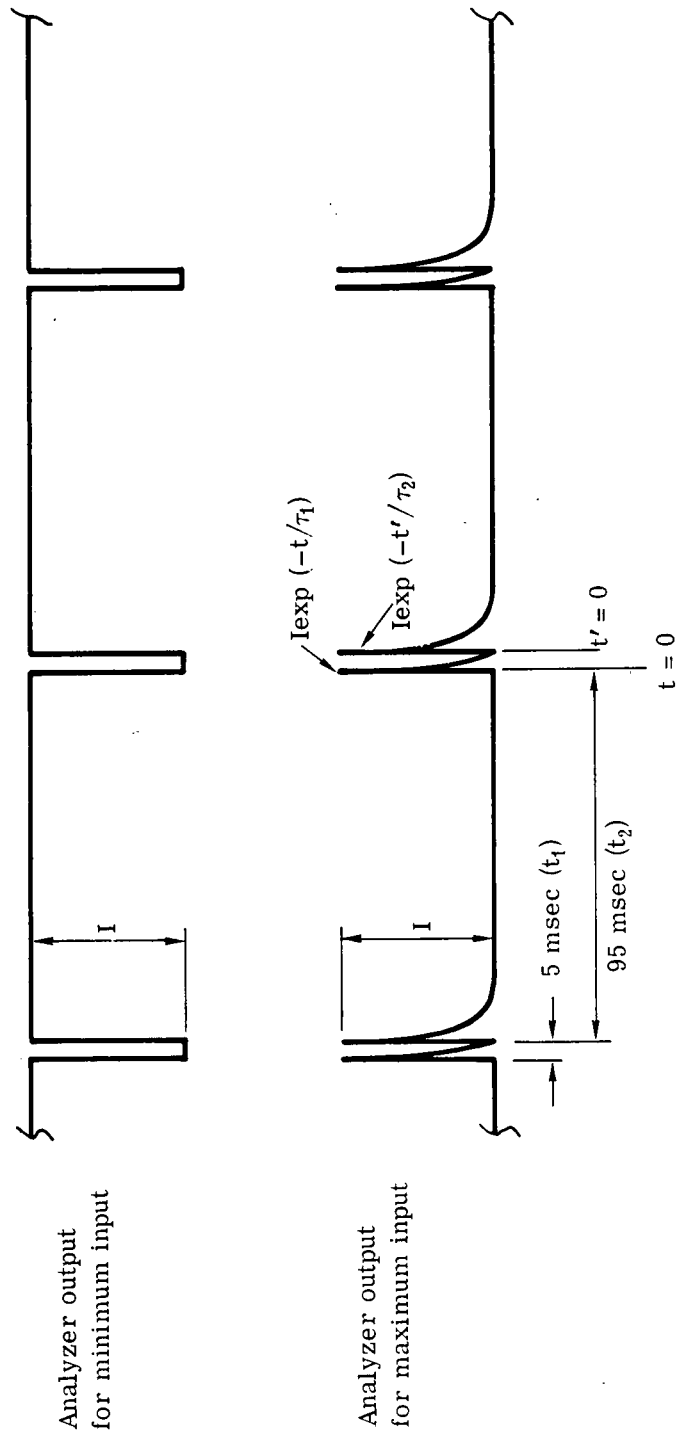


Fig. 2-5 Analyzer outputs for high contrast inputs

It follows from (4) that the decay time constant, τ_2 , must be 1.9 milliseconds to yield an average contrast ratio of 50. Previous PROM devices have shown that 100 ergs/cm^2 is required to decay the readout light to the e^{-1} point. Using this sensitivity data it follows that a non-coherent input intensity of $5 \text{ milliwatts/cm}^2$ is required to produce a coherent output contrast ratio of 50.

If the readout is not viewed continuously but sampled as for example when snapshot photographs are made of the coherent output image a much higher output contrast ratio can be obtained for a given noncoherent input light intensity by sampling the readout near the end of a 100 millisecond frame period.

2.5 Optimum Device Geometry For a Noncoherent-to-Coherent Converter -

In choosing a device geometry to meet the requirement for a real time noncoherent-to-coherent converter it was felt that a configuration in which the noncoherent write-in and coherent readout radiations were directed through opposite faces of the device was most desirable. Therefore, it was decided to use the configuration of Figure 2-1(a) in which one face of the $\text{Bi}_{12}\text{SiO}_{20}$ crystal would be coated with a dichroic reflector designed to transmit wavelengths in the blue and near UV and to reflect wavelengths in the red (specifically 632.8 nm).

The noncoherent radiation is introduced into the crystal after passing through a transparent platinum electrode, a 3 micrometer layer of Parylene, and the dichroic layer. Coherent readout radiation enters through the opposite transparent platinum electrode and Parylene layer, travels twice through the $\text{Bi}_{12}\text{SiO}_{20}$ crystal due to a reflection off the dichroic layer, and exits back through platinum electrode. By using this device design all of the coherent readout optics can be separated from the non-coherent write-in optics. Furthermore two passes through the crystal doubles the electro-optic modulation introduced into the readout beam.

3. GROWTH OF $\text{Bi}_{12}\text{SiO}_{20}$ CRYSTALS

3.1 Procedure -

Since $\text{Bi}_{12}\text{SiO}_{20}$ is congruently melting material, the Czochralski technique can be employed effectively to grow large single crystals in relatively short times with no variation in stoichiometry. The details of this particular growth process are given in this section and shown in Figure 3-1.

Seed crystals can be obtained by spontaneous nucleation on a gold rod. However, it is preferable to use seeds cut from previously grown crystals. Crystals were first x-rayed by Laue reflection to determine the (100) direction. They were then mounted and sliced so as to obtain seeds from which subsequent crystals could be grown on the (100) axis. The Laue pattern of the (100) direction is shown in Figure 3-2. In this way, it was possible to control both the orientation and sign of the optical activity since these properties are governed by the respective properties of the seed. Seeds are attached to a gold pullrod for growth.

Stoichiometric quantities of Bi_2O_3 (6 moles) and SiO_2 (1 mole) are physically mixed and reacted at $1,000^\circ\text{C}$ in a gold crucible to ensure homogeneity of the melt. In cases where ultrapure material is desired, Bi_2O_3 can be prepared in the laboratory, having less than 2 ppm total metallic impurities.

A two-zone growth furnace is used to reduce any temperature gradients near the surface of the melt and to allow a long crystal to be maintained at a uniform temperature during growth. This results in a very slow, controlled cooling of the crystal and minimizes built-in strain. The gold crucible and its contents are isolated from the furnace windings by a 99.9 percent pure alumina tube which is gas impermeable. This permits use of a controlled atmosphere, usually argon or oxygen, and prevents atmospheric contamination.

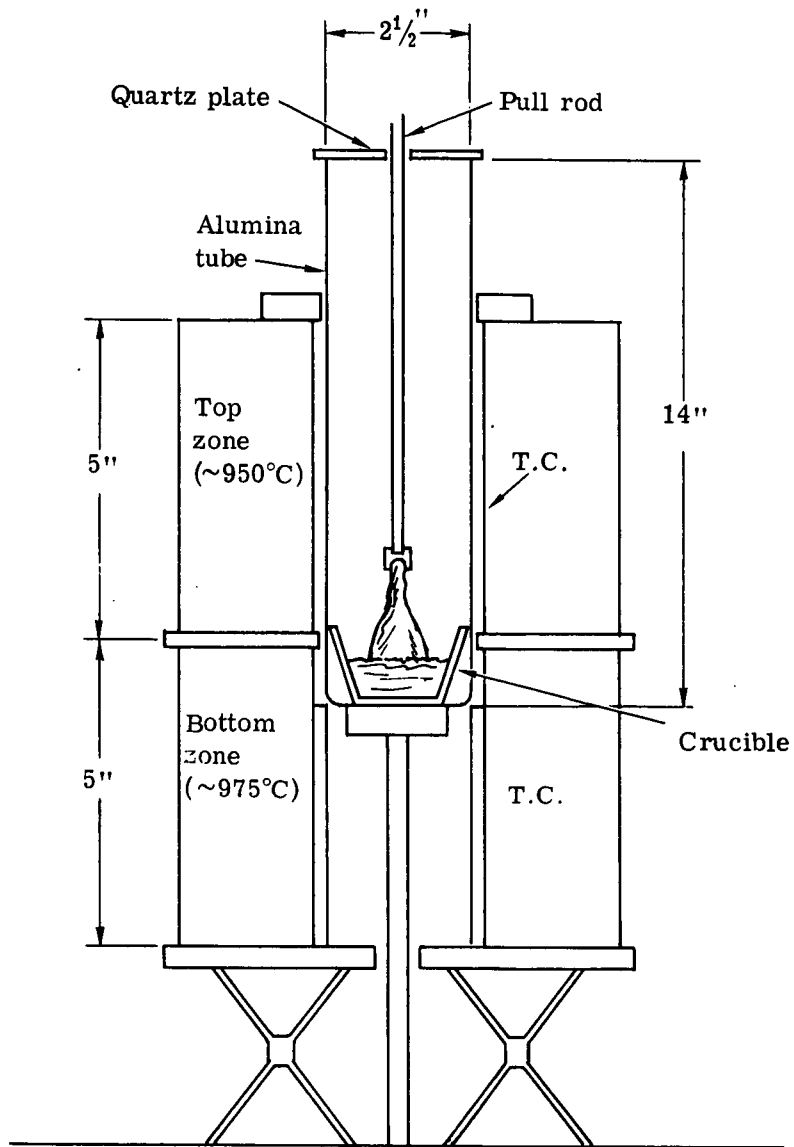


Fig. 3-1 Apparatus for growing electro-optic material

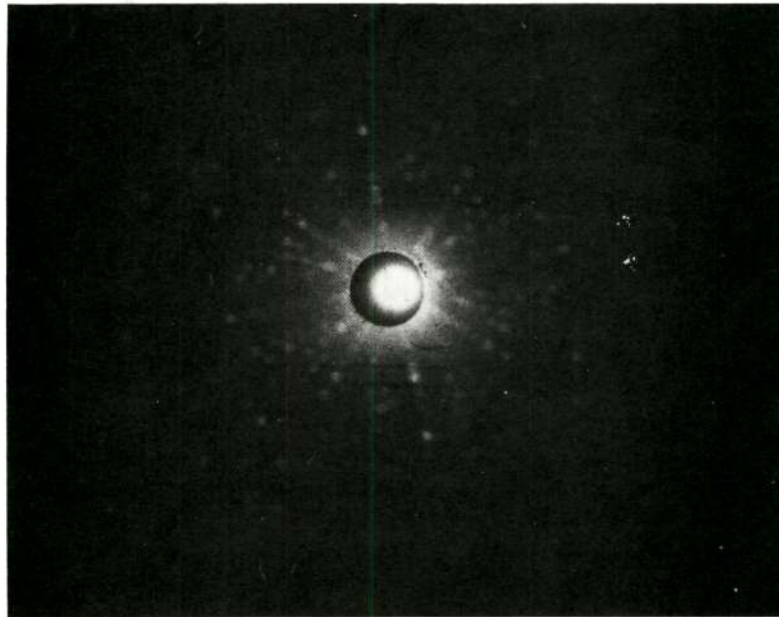


Fig. 3-2 Laue pattern of $\text{Bi}_{12}\text{SiO}_{20}$ crystal

Reproduced from
best available copy. 

All temperature programming is accomplished by externally placed chromel/alumel thermocouples located adjacent to the exterior of the alumina tube. Furnace control is achieved by step-less SCR power sources which maintain furnace temperatures to $\pm 1.0^{\circ}\text{C}$ and melt temperatures to $\pm 0.1^{\circ}\text{C}$. Melt temperatures are not monitored during growth since Bi_2O_3 is an excellent solvent and contamination of the melt would result. Actual furnace temperatures during growth are approximately 950°C for the top zone and approximately 975°C for the bottom zone. Zone separation is achieved with a 0.5-inch-thick fire-brick baffle. Crucible gradients are controlled manually by laboratory jacks that can either raise or lower the furnaces while keeping the alumina tube and its contents stationary. The gradient is adjusted such that the growing crystal emerges from the melt with completely formed crystallographic faces. In addition, laboratory temperatures are maintained to $\pm 5.0^{\circ}\text{C}$ by oversized heaters and air conditioners since room temperature fluctuations of $\pm 10^{\circ}\text{C}$ during growth induce crystal strain.

Typical pulling parameters under these conditions are a pull rate of 0.3 inch per hour with a rotation rate of 50 to 200 revolutions per minute. When these parameters are used, crystals up to 3 centimeters in diameter by 6 centimeters long can be grown. Figure (3-3) is a photograph of a $\text{Bi}_{12}\text{SiO}_{20}$ ingot cut off at the seed end.

Seven $\text{Bi}_{12}\text{SiO}_{20}$ ingots were pulled from (100) oriented seeds during the course of this work. The largest weighed about 100 grams and its maximum diameter exceeded 1". Good crystal growth is characterized by four fold symmetry consisting of the crystal sides in the form of pronounced "flats". Visual examination of the as grown crystals reveals a number of features. The color in room light can vary from a light amber to a reddish brown. A number of voids, point defects which look

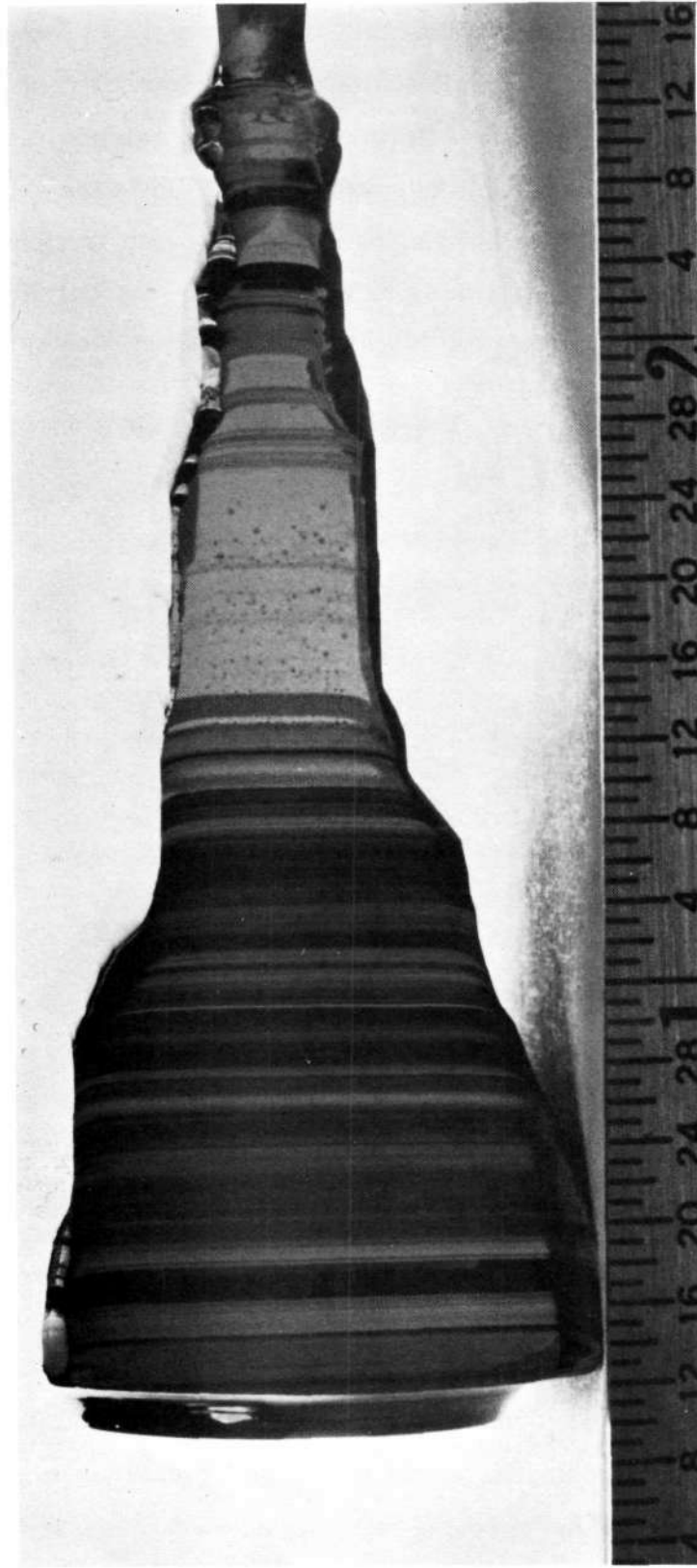


Fig. 3-3 As grown $\text{Bi}_{12}\text{SiO}_{20}$ crystal

like particles of grit, and linear boundaries, generally running parallel to the crystal axis, can be observed internally.

Table (3-1) tabulates the semi-quantitative spectrographic analysis from two samples of $\text{Bi}_{12}\text{SiO}_{20}$. Sample amber (A) is from a pulled crystal. Sample green (B) is one from the solidified melt left in the gold crucible. The only significant differences are in the concentrations of gold and iron. The gold concentration is understood in terms of gold leaching in from the crucible. Iron probably has a distribution coefficient greater than 1 in this system.

Pulled Ingot	Amber (A) ppm	Green (B) ppm
Al	2	7
Ag	0.1	0.5
Au	10	40
Ca	1	1
Cu	6	6
Fe	90	10
Mg	1	5
Mn	0.5	0.2
Ti	-	1

Bi and Si are the major constituents.

Table 3-1 Spectrographic Analysis of $\text{Bi}_{12}\text{SiO}_{20}$

3.2 Crystal Strain -

One feature of the early crystal growth was the tendency for the ingot to crack as it was being removed from the furnace or during cooldown as it approached room temperature. Since $\text{Bi}_{12}\text{SiO}_{20}$ does not have a plane of cleavage, the cracking was random; i. e., like glass.

Cracking of $\text{Bi}_{12}\text{SiO}_{20}$ has its origin in the lattice structure of the crystal, specifically the large thermal expansion coefficient which is of the order of six times that of germanium. Other factors contributing to cracking are the large piezoelectric effect in $\text{Bi}_{12}\text{SiO}_{20}$ and the necessity of adding the second oxide phase (SiO_2) in order to stabilize the B.C. cubic structure. This oxide is known to change the lattice constant [10].

This problem, to a large extent, was overcome by annealing the crystal, in situ, during cooldown. This generally consisted of a uniform cooldown from the growth temperature over a period of 72 hours. From this annealing procedure crystals were generally removed from the furnace intact.

Strains and stresses were further evaluated by observation of birefringence in polished (100) oriented wafers and by chemical etching to reveal pits and various other defects. Since $\text{Bi}_{12}\text{SiO}_{20}$ single crystal is optically isotropic, no birefringence should occur in unstrained crystals when viewed in transparent light between crossed polarizers. Such was not the case as birefringence, caused by strain, is always observed, in varying amounts, in polished wafers. It is convenient to avoid the effect of optical activity in $\text{Bi}_{12}\text{SiO}_{20}$ when viewing wafers in monochromatic light between crossed polarizers either for birefringence or PROM device operation. This is the basic reason why the dichroic reflector was evaporated onto one surface of the wafer. This makes it efficient to view the wafer by reflection. The optical rotation is directionally dependent and the rotation during one pass is reversed and cancelled in reflection. Birefringent strain is always more pronounced in thicker wafers. An etch consisting of one part HCl to ten parts H_2O for five to ten minutes was found to be very effective in chemically etching the (100) surface. This etch was used in two ways. It was used as an etch to chemically remove surface damage caused by grinding and rough polish. Such surface damage is known to result in surface stresses which in seeds is detrimental to crystal nucleation and in thin wafers can cause bending. Thus, seeds used in crystal growth and wafers before final polish are etched in this solution.

This dilute HCl etch was also found to be very effective in revealing pits, the majority of which are believed to be due to dislocations.

Figure (3-4) is a photograph of two polished (100) oriented wafers which have been etched for ten minutes. The center of the wafer is most heavily etched and there are four etched regions near the edge oriented in the (100) radial directions. Usually etching has been randomly distributed in the surface of the wafer. However, when symmetrically etched patterns were observed, they always had the 4-fold symmetry as shown in the patterns. Closer examination of the etching pattern reveals that it is made up of 4-fold symmetric pits plus other shaped pits. The square etch pits are also characterized by their occurrence in pairs, one on each surface of the wafer. A photograph of this is seen in Figure (3-5) where each etch pit (A) has a counterpart on the opposite surface, the smaller pit (B). This indicates a line defect, probably an edge dislocation. The smaller etch pits having the appearance of dark oval bands could be caused by point defects. Figure (3-6) is a photograph of etch pits aligned in a straight line. The parallel shadow is the line of pits in the opposite face. This defect plane may be caused by a dislocation loop.

Surface etching has revealed a large concentration of point and line defects in $\text{Bi}_{12}\text{SiO}_{20}$. Figure (3-4) indicates that the center of the ingot is most highly strained and this observation is supported by strain birefringence observations.

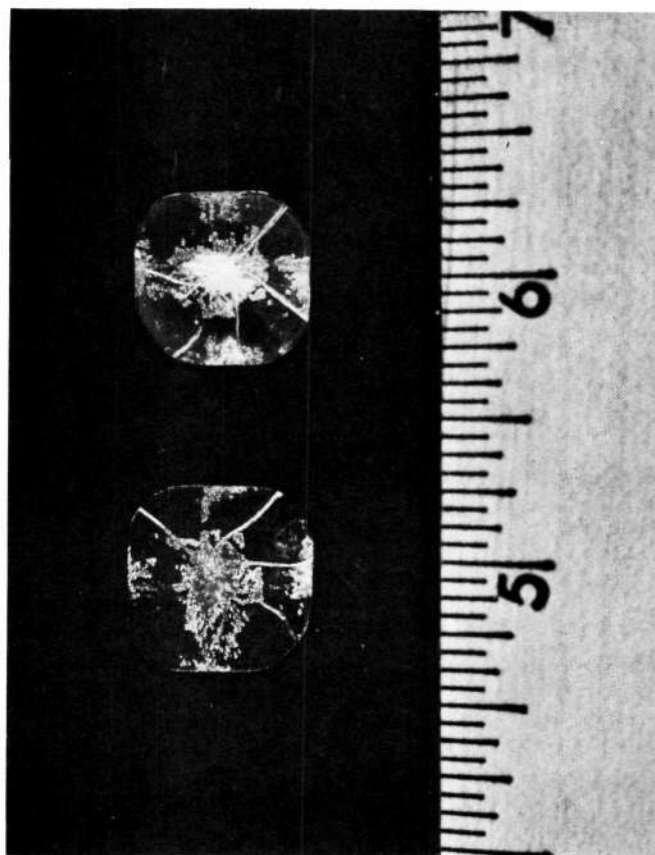


Fig. 3-4 Polished and etched wafers

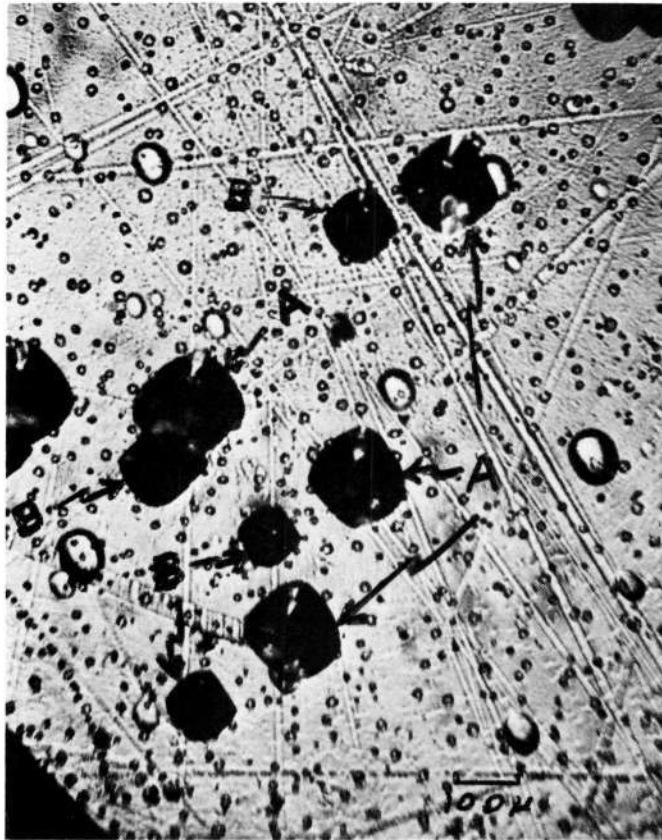


Fig. 3-5 Etch patterns in $\text{Bi}_{12}\text{SiO}_{20}$



Fig. 3-6 Etch patterns in Bi₁₂SiO₂₀

4. DEVICE FABRICATION AND EVALUATION

Devices of the type pictured in operation in Figure 4-1 were fabricated and evaluated. Device fabrication consisted of a number of steps beyond the $\text{Bi}_{12}\text{SiO}_{20}$ single crystal growth described in the last section.

4.1 Slicing and Polishing -

Ingots were first oriented and mounted on blocks with the (100) axis perpendicular to the direction of slicing. Wafers, approximately .030" were sliced with the inner diameter of a hollow ground cutting wheel.

The wafers were then ground and etched in dilute HCl. During etching, care must be taken to avoid pitting the wafer to the point where it can't be polished flat. The final polish was made with a silica gel. The wafer is then removed from the block and re-cemented to expose and polish the other side. Generally, the wafers could be polished with surfaces parallel to within a few waves. The silica gel always leaves a small residue of grit on the surface which couldn't be cleaned away.

4.2 Electrical and Optical Evaluation of Wafers -

Current voltage characteristics were recorded using a Cary electrometer. Measurements were made between faces of typical polished $\text{Bi}_{12}\text{SiO}_{20}$ wafers. Electrodes were of evaporated platinum. Typical of insulators, when the voltage is first applied, in a step function, a rather large current flows. The current gradually decreases and after several minutes the sample reaches a steady state condition. After about fifteen minutes, the d.c. is measured. Typical values of resistivity are 10^{14} ohm-cm at 100 volts and 5×10^{13} ohm-cm at 1000 volts applied.

Birefringent strain, interference fringes and surface defects as they affected device operation were subsequently evaluated, after the dichroic layer was evaporated, in reflected HeNe laser light.

4.3 Dichroic Reflector -

The multilayer dielectric coating consists of nine layers alternating between MgF_2 ($n = 1.38$) and ZnS ($n = 2.35$). The coating is evaporated

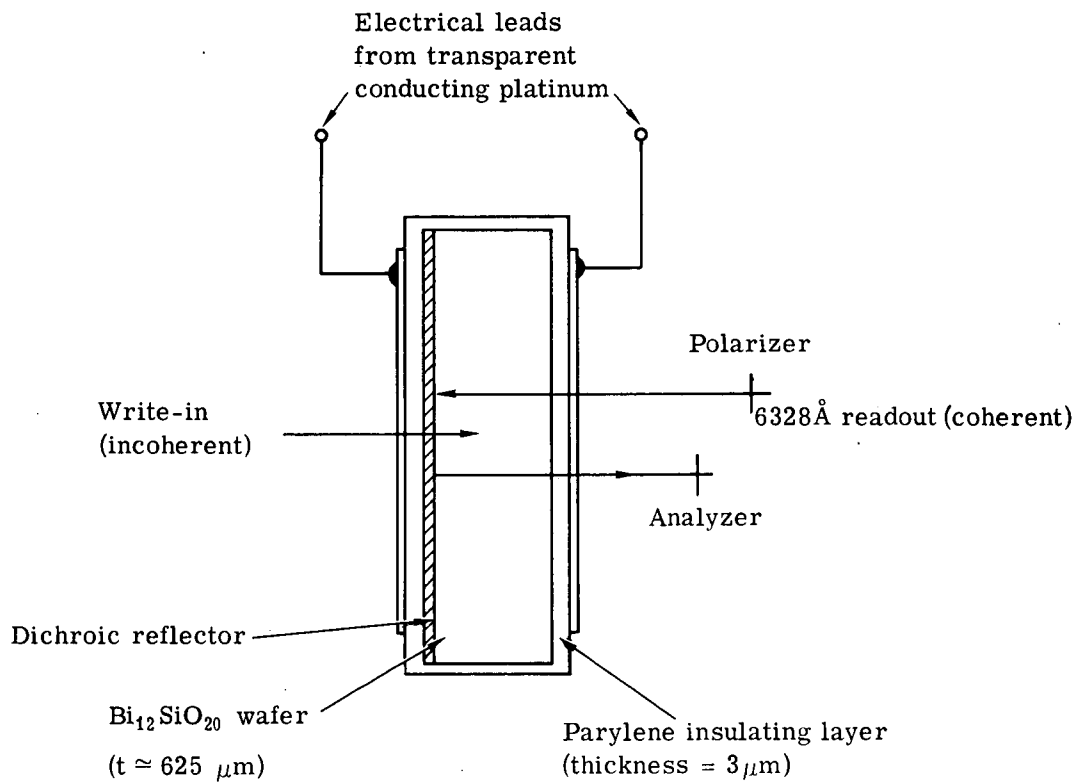


Fig. 4-1 Optical to optical interface device

directly onto one of the polished $\text{Bi}_{12}\text{SiO}_{20}$ surfaces. The coating is designed to be 95% reflecting at a wavelength of 6328 \AA and about 95% transmitting between 4200 \AA and 4700 \AA . The cutoff is at 5300 \AA .

4.4 Parylene Coatings -

The Parylene coating over the $\text{Bi}_{12}\text{SiO}_{20}$ provided the insulating layer which served as the voltage divider between the low resistivity write-in regions and the high resistivity non-write-in regions of the device. Parylene, a generic name of a polymer developed by Union Carbide Corporation, is produced by vapor-phase polymerization and deposition of para-xylene. The deposition apparatus is shown in Figure 4-2. The wafers to be coated are hung inside the deposition chamber. The coating rate is about one micron per hour. The resistivity of Parylene has been measured and is in excess of 10^{17} ohm-cm. The dielectric constant is 2.6. These properties and the fact that it is a plastic which can be deposited on $\text{Bi}_{12}\text{SiO}_{20}$ at room temperature make it suitable to be used as the insulating film required for the present mode of operation.

Figure 4-3 is a photograph of the electron diffraction pattern of a three micron Parylene film on a $\text{Bi}_{12}\text{SiO}_{20}$ wafer.

4.5 Completion of the Device -

The device was completed by evaporating a 60% transmitting film of platinum on both faces to serve as electrodes. At this transmission the surface resistivity is less than 1000 ohm/square. The device was then mounted on a plastic disk which could be installed on a holder in an optical bench.

4.6 Device Evaluation Techniques -

The experimental setup employed during much of this work is shown in Figure 4-4.

The Kepco O.P.S. 2000, proved quite useful as the high voltage pulser. It has a rise time of 1000 volts per millisecond.

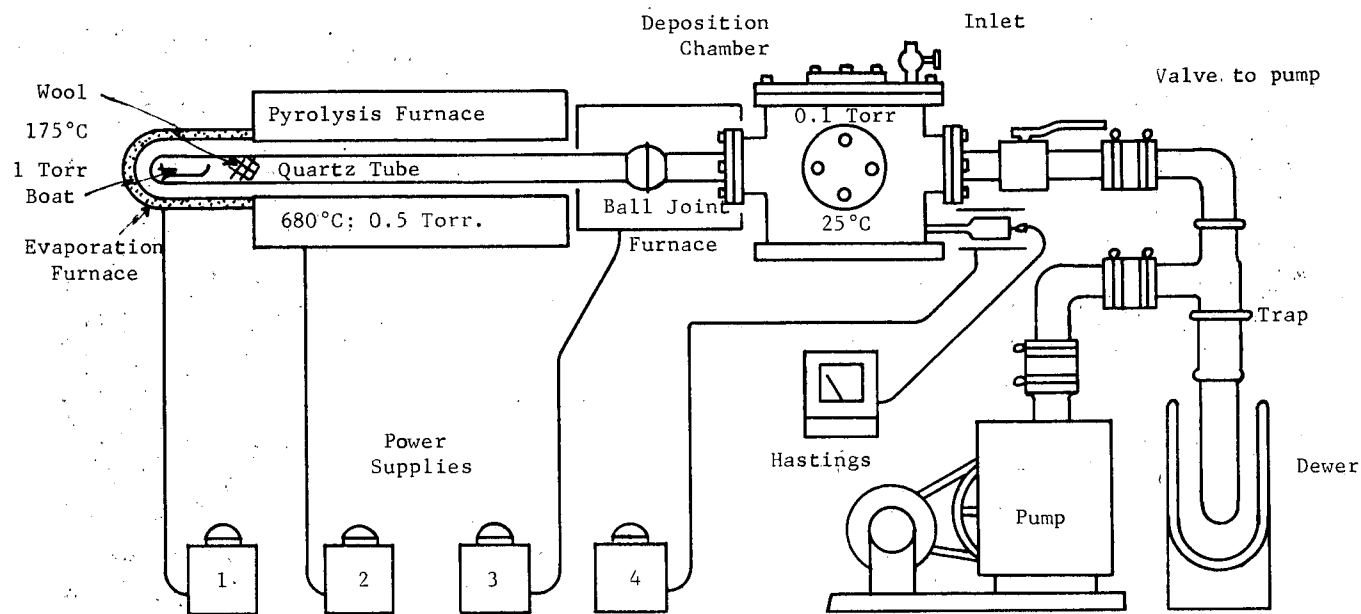


Fig. 4-2 Parylene deposition apparatus

Reproduced from
best available copy.



2μ

Fig. 4-3 Electron diffraction pattern for Parylene

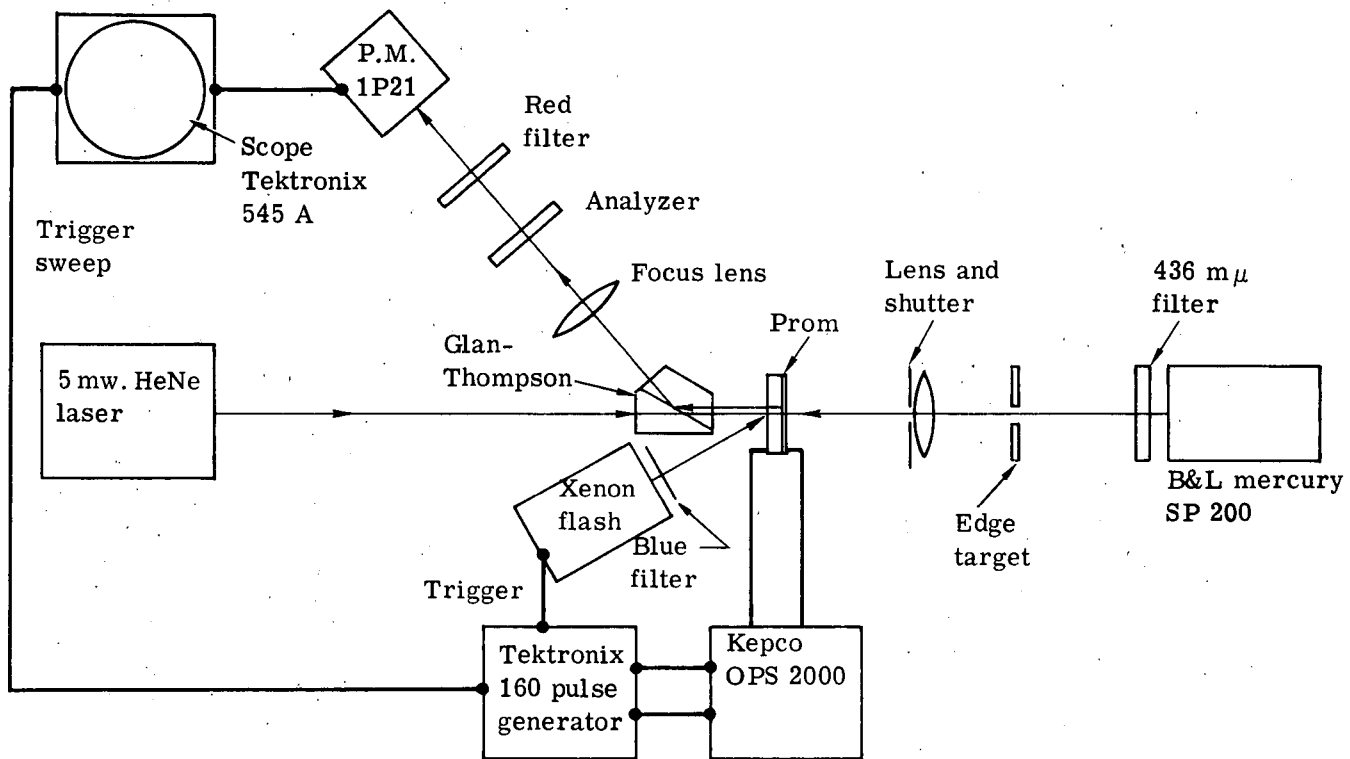


Fig. 4-4 Experimental setup for device evaluation

4.7 Contrast Ratio -

A contrast ratio measurement was made on a .030" thick device with a total Parylene thickness of six microns. The active area was around 3 cm^2 . When the converter is operated in a real time mode, the contrast ratio (C.R.) is defined as the ratio of the average intensity of the read out image in the dark struck area to that in the light struck area as seen by a photodetector in the plane of the read out image. When recorded in real time on an oscilloscope, the C.R. becomes approximately equal to ratio of the discharge times with and without write-in light, as derived in section 2 and depicted in Figure 2-5.

The applied voltage was 1500 volts, the pulse was two milliseconds in width at a frequency of 20 cycles per second. The device was xenon flashed at the peak of the pulse and between pulses. The converter is effectively shorted and in a state to accomplish optical conversion. An "edge" target blanks off about half the active area of the device so that blue incoherent write-in light, of 10 mw/cm^2 intensity, is incident on the other half. Thus, the reconstructed image is half dark and half light (the negative of the write-in). The photomultiplier, positioned in the plane of the read out image is moved across the boundary and the signals are compared on an oscilloscope to determine the contrast as recorded in Figure 4-5. Notice the similarity of the experimental trace to the predicted one of Figure 2-5.

4.8 Sensitivity -

The absorption coefficient and the wavelength dependence on sensitivity were measured on a .013" thick device. Four mercury lines were used. The results are graphed in Figure 4-6. The peak sensitivity occurs around 400 nm which is reasonable when the absorption coefficient is considered. At 400 nm, $\alpha \approx 10^2$ and $\alpha t \approx 3$. Therefore, at 400 nm, practically all of the light has been absorbed exponentially throughout the .013" thick device. It is reasonable to expect a peak in the sensitivity under these conditions. The quantum efficiency (i.e., the number of charges at the $\text{Bi}_{12}\text{SiO}_{20}$ - Parylene interface which are

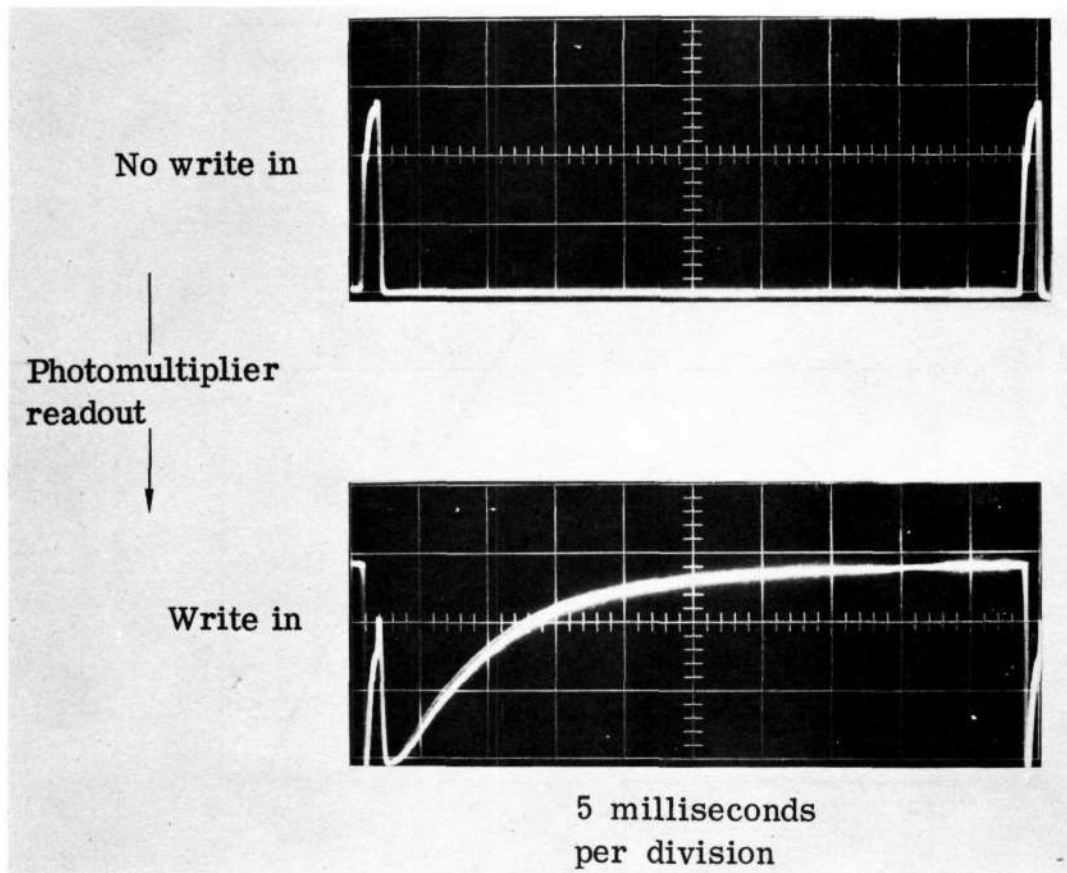


Fig. 4-5 Experimental discharge trace

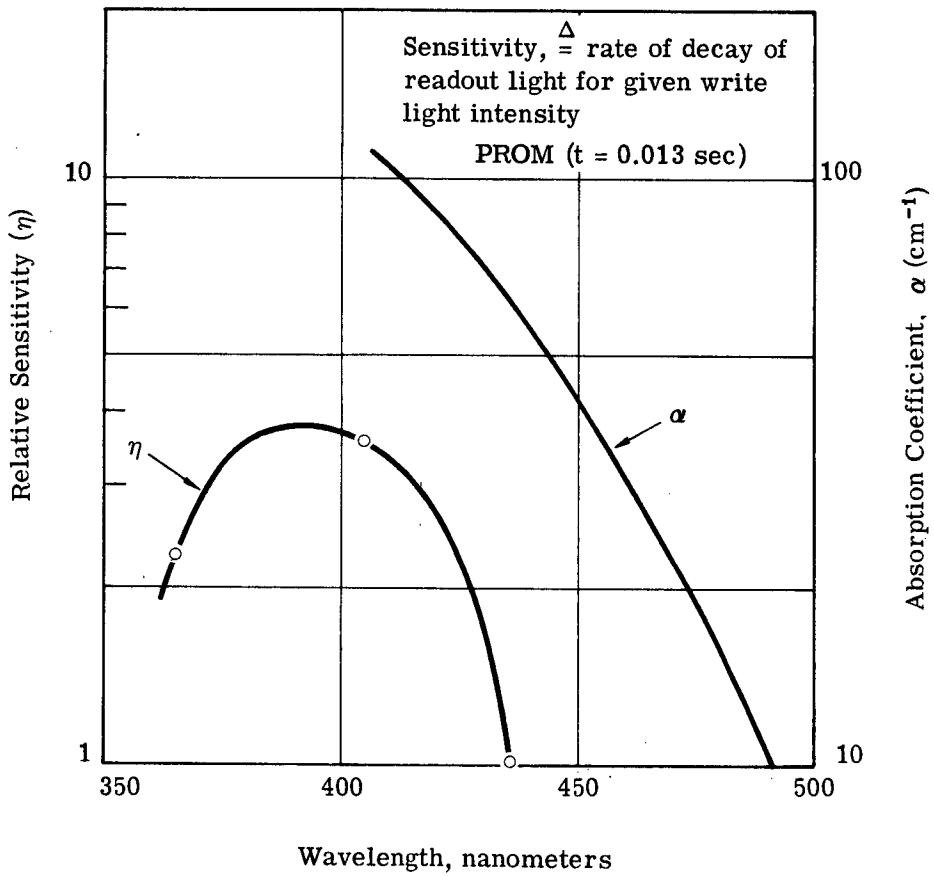


Fig. 4-6 Absorption coefficient and spectral sensitivity of device

discharged per unit incident photon of write-in light) has been calculated (see Appendix) using measurements made at 436 nm and found to be 22 %.

4.9 Additional Measurements -

Additional measurements were made of the electron transit time and the electron mobility. These measurements were made by generating carriers with a 5 μ s pulse of 366 nm light. The transit time was measured by recording the electro-optic change of read out light from the 6328 Å laser with a photodetector (essentially the discharge time of the device). The transit time of electrons measured by this method was around 20 μ s for a .015" thick device. The mobility as calculated from the relationship $\mu_e = L^2 / TV_o$ was .025 cm²/volt-sec. Where L is device thickness, T is transit time, and V_o is applied voltage.

5. ELECTRONIC DRIVE EQUIPMENT

A block diagram of the electronic drive equipment required to operate the converter is shown in Figure 5-1. It consists of three basic components: a programmable power supply to provide the high voltage bias pulse for the converter during the erase/prime phase of its operating cycle and to act as an electrical short circuit during the write/read phase; a pulse generator to provide the desired pulse waveform (width and amplitude) at a preset replate (10 pulses per second) for subsequent amplification by the programmable power supply; and a xenon flash lamp with associated power supply to generate a high intensity, short duration pulse of light for erasing the converter every 100 milliseconds. A detailed description of these components follows.

5.1 Programmable Power Supply -

A Kepco Model OPS2000 operational power supply was used as the programmable source of high voltage. It contains a self-powered operational power amplifier and d-c power supply. It utilizes a high voltage vacuum tube, together with a d-c coupled transistor amplifier. The output voltage amplitude and waveform can be programmed by applying an appropriate low voltage signal to the unit. The output slewing rate of 1000 volts/millisecond is the limiting factor in determining the minimum period of the erase/prime cycle. The full-scale output capability of the supply is 2000 volts and 10 milliamp.

5.2 Pulse Generator -

The pulse generator for driving the programmable power supply was assembled using Motorola digital integrated circuits. The block on Figure 5-1 representing the pulse generator has been enlarged so that the electrical schematic of the unit can be depicted.

The specific Motorola units employed are described in Table 5-1. The MC832, MC858, and MC845 units utilize diode-transistor logic (DTL) and the MC 7400 unit employs transistor-transistor logic (TTL).

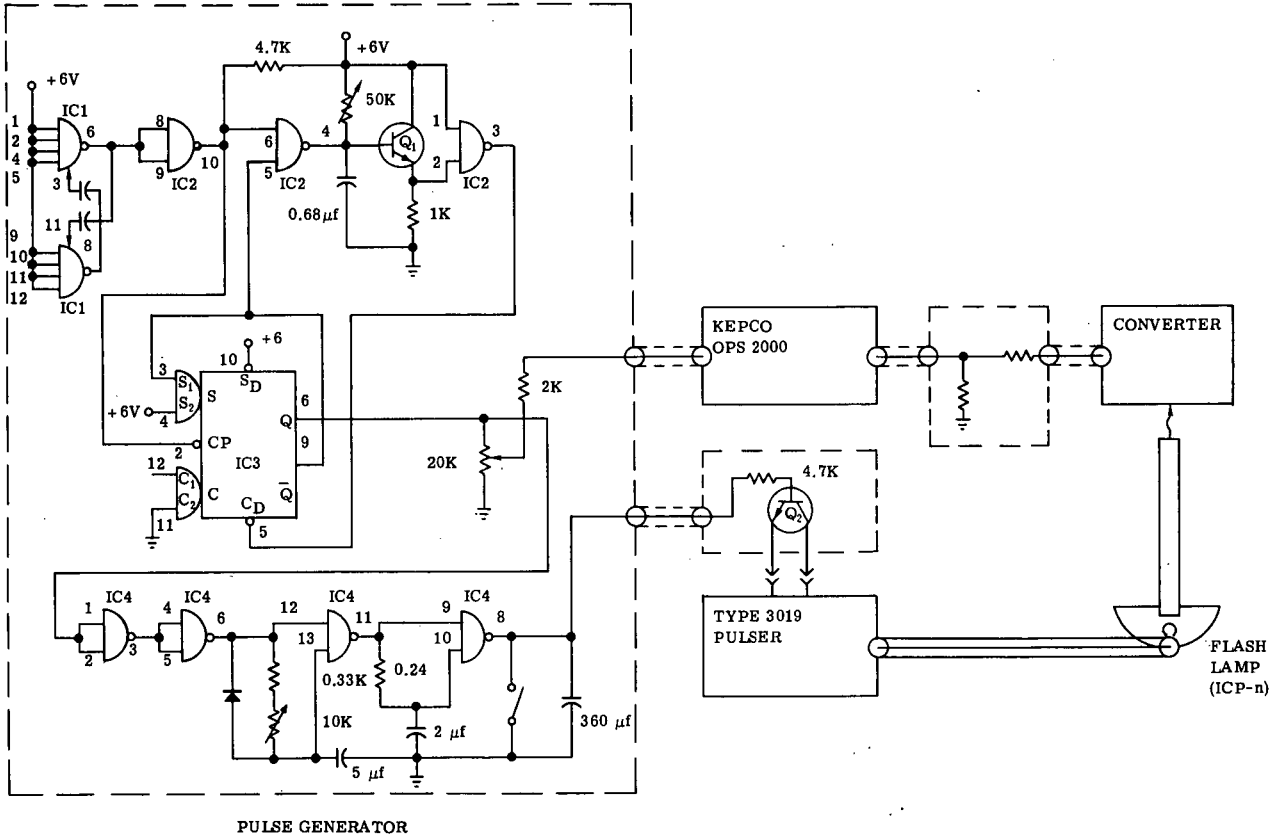


Fig. 5-1 Electronic drive schematic for optical interface device

Module IC1 is used to form a 10 Hz oscillator which sets the replate of the converter. The IC2 module in conjunction with transistor Q1 and module IC3 generates a variable width pulse of voltage which is dropped across a 20K voltage divider. The output of the voltage divider feeds the programmable power supply. After amplification by the power supply this voltage waveform is applied to the converter through a 200K current limiting resistor.

Module IC4 is used to generate a pulse delayed in time from the biasing pulse. A 10K resistor is used to adjust the time delay and the resulting waveform is used as a strobe signal for the flash lamp. Transistor Q₂ is operated as a solid-state switch to simulate a contact closure to initiate the flashing sequence.

5.3 Xenon Flashlamp and Power Supply -

A U.S. Scientific Instruments, Inc. Type 3019 Pulser and ICP-n compact arc type, pulsed xenon flash lamp were used for the flash erase system. The lamp was placed in a parabolic reflector and a mirrored cover plate was placed over the reflector opening to confine the illumination. A Bendix (Mosaic Fabrications Division) flexible glass fiber light pipe was used to couple the flash output to the converter (see Figure 6-1 and 6-2). The Pulser was operated in the externally triggered mode with the Q₂ output from the pulse generator applied across the contact closure terminals.

<u>Circuit I.D. No.</u>	<u>Manuf. No. (Motorola)</u>	<u>Description</u>
IC1	MC832	Dual 4-input buffer
IC2	MC858	Quad 2-input nand power gate
IC3	MC845	Clocked flip-flop
IC4	MC7400	Quad 2-input nand gate

Table 5-1 - Pulse Generator Logic Module Specs.

6. PERFORMANCE TESTS

6.1 System Requirements -

The performance goals set for this basic optical-to-optical interface device included the ability to accept as an input reflected (noncoherent) light from a small object illuminated by standard photoflood lamps. The coherent readout image was to be Fourier transformable so that a power spectra could be generated using a suitable transforming lens. Furthermore, a coherent image of the input scene was to appear on a screen located in the rear focal plane of a subsequent inverse transforming lens.

Furthermore it was required that the device have sufficient resolving power to convert a 64 x 64 block checkerboard such that all squares could be easily discernible and countable in the displayed coherent output image. Additional design goals included an output contrast ratio of 50:1, an image generation time of 100 milliseconds, and an optical readout transfer efficiency of at least 5% (measured as the percent of the coherent light intensity entering the device which appeared in the output display).

6.2 Optical Apparatus -

The optical systems used for evaluating the operation of the PROM device as an optical-to-optical interface device (noncoherent-to-coherent converter) are diagrammed in Figures 6-1 and 6-2. Figure 6-1 shows the system for write-in of transmission targets while Figure 6-2 shows the system for testing write-in of reflective targets. Table 6-1 summarizes, and describes in detail, the key elements in the test systems.

The transmission write-in system (Figure 6-1) uses a 200 watt high pressure mercury arc, with light collecting optics as the incoherent illuminating source. The target is illuminated through an interference filter having a passband centered at 436nm. The filter is used to minimize chromatic aberration effects in the write-in image within the photosensitive electro-optic crystal. The imaging lens which was set at F/4 to provide adequate depth of focus, images the target onto the converter. In the transmission mode, all targets were imaged onto the converter with unity magnification. The lens was mounted in a holder sitting on a triangular optical rail, which allowed coarse focusing of the input image. Fine focus adjust-

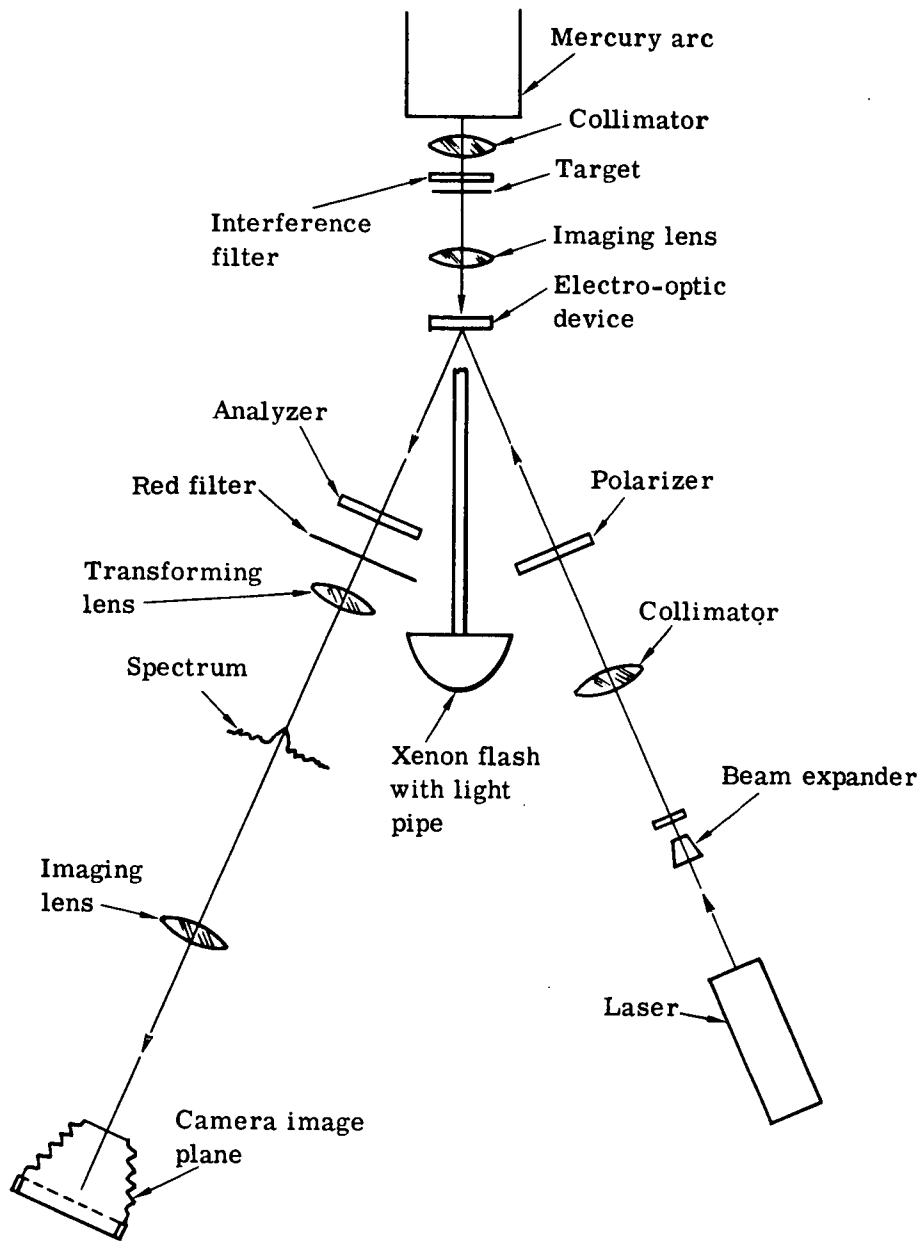


Fig. 6-1 Optical apparatus for performance testing OID (transparent targets)

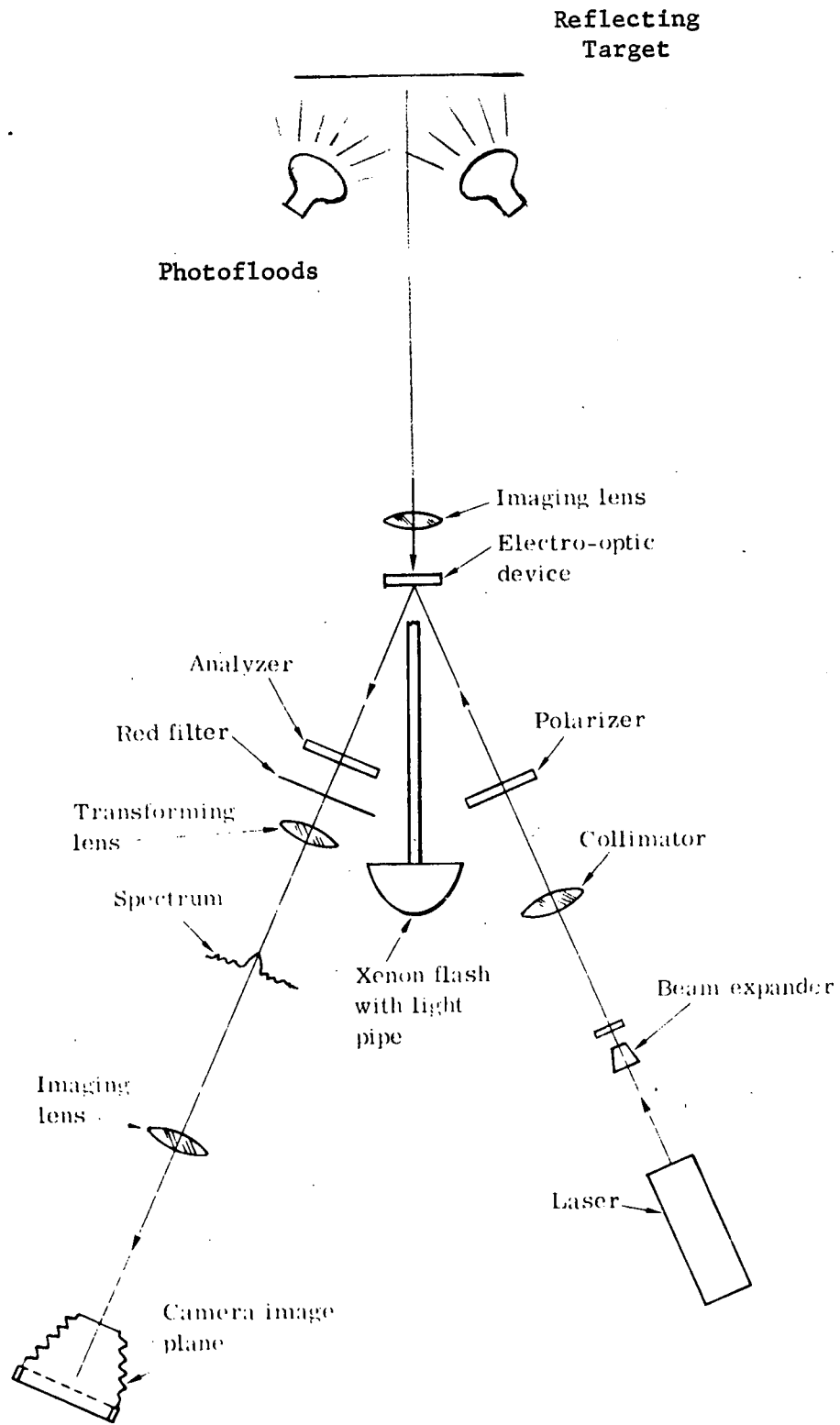


Fig. 6-2 Optical apparatus for performance testing OID (reflective targets)

ments were made using the focusing mechanism of the lens. Initial target focusing was performed by maximizing the apparent sharpness of the image on the rear surface of the converter. Final focus adjustments were made while viewing either the readout image or the readout coherent power spectrum.

The readout system was used for both the transmission and reflection modes of write in. The 5mw helium-neon laser was expanded and collimated to give a beam diameter of approximately 1.5 centimeters. This beam size covered the useful converter width without overlap onto the edges or silver paste electrodes. A polarizer was inserted between the laser and the converter to improve the polarization of the readout beam. The beam also passes through a circular diaphragm (not shown) to block stray laser light. After exiting from the converter, the readout beam passes through an analyzer whose plane of acceptance is rotated approximately 90 degrees relative to the polarizer. The beam then passes through a wideband red filter (Kodak Wratten #25) to block stray blue light coming either from the write-in source or the xenon flash. The transform lens, which has a 380 mm focal length, was set so that the converter was in its front focal plane. The spectrum is observed in the back focal plane of the transforming lens with a scale of 2.4 millimeters corresponding to an object frequency of 10 cycles/millimeter. When photographs were made of the spectrum, a magnification was obtained by properly inserting a lens to form an enlarged image in the camera. Retransformation to obtain an intensity image is performed using a second 380 mm lens immediately after the spectrum, with the image appearing in its back focal plane. All photos were taken with a Graflex Camera having a 4" x 5" Polaroid back. Contrast measurements were made on the images by replacing the camera back with a photometer mounted on a cross slide.

The xenon flash, which was used for erasing and priming the converter before each new exposure, consisted of a flash lamp mounted in a semiparabolic reflector. A flat mirror with a 1/2 inch hole cut in its center was

attached to the front of the reflector. A 1/2 inch diameter 12 inch long fiber optic light pipe was inserted in the hole. Since the end of the light pipe was located near the focus of the parabola, a large percentage of the flash light is delivered down the light pipe, and directed towards the converter, with the output end of the pipe placed approximately two inches from the converter. This arrangement not only efficiently collects the light, but also greatly restricts bothersome strong light from the flash.

The reflection mode of write-in (Figure 6-2) replaces the mercury arc with two 650 watt photo flood lamps illuminating a reflecting target. For convenience, a large reflecting object was imaged down onto the converter with a 10 to 1 demagnification. The rest of the write-in and readout system was identical to the transmission mode system.

6.3 Initial Filtering Experiments -

The general purpose of the optical-to-optical interface device is to take an incoherently illuminated image and spatially modulate the intensity of a coherent light beam in real time so that its intensity is proportional to the original image. This coherent intensity distribution may then be optically Fourier transformed and the resulting spectrum spatially filtered to perform Fourier synthesis operations as in a conventional coherent processor. A standard demonstration of the Fourier synthesis properties of a coherent optical processor was carried out with the PROM using a transmission write-in and readout¹ system.

A crossed grating having a frequency of 10 lines/mm was used as a target. When the grating was imaged onto the PROM, with the PROM operating in the d-c mode (as described in section 2), the grating diffraction spectrum was observed in the transform plane. The exposure time was adjusted, using a shutter in front of the arc lamp, for maximum observable brightness in the spectral orders. The optimized spectrum was then inverted to give an image, which was recorded on Polaroid Type 57 Positive/Negative film. Figure 6-3 is an enlargement of the grating image.

¹. The PROM device tested had no internal dichroic reflector therefore was not readout in reflex.

Reproduced from
best available copy.

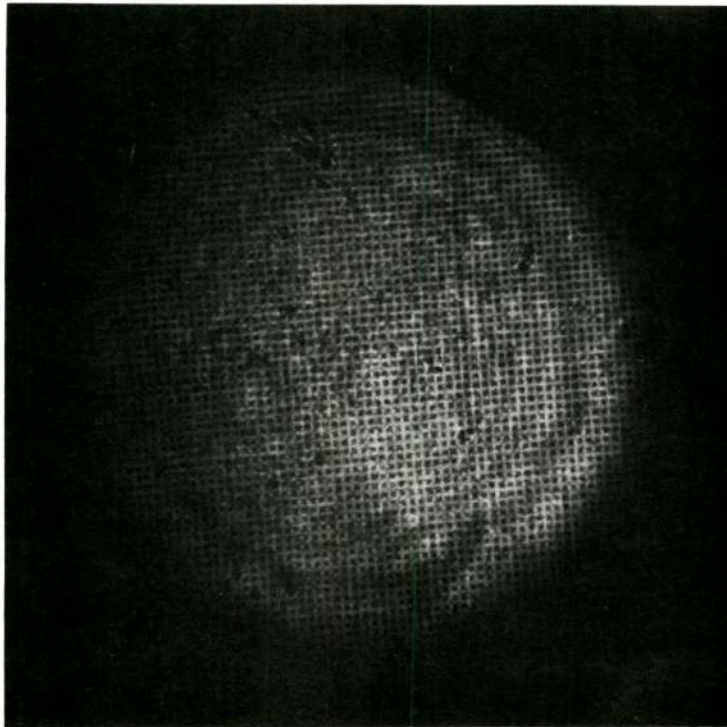


Fig. 6-3 OID output image of 10 lp/mm crossed grating

The non-uniform brightness across the image is mostly due to the Gaussian intensity profile of the readout beam. There are a considerable number of dust and dirt spots causing ringing in the image. This effect occurs in all optical systems using coherent illumination, with many of the dirt specks on the various optical elements. The high frequency low contrast fringe pattern running diagonally in the background is due to interference between the main image wave and secondary reflected wave.

The effect of the interference patterns would be reduced if a lower reflectivity front electrode could be implemented (such as replacing the platinum electrode with a more transmissive coating such as indium oxide), or by reducing the temporal coherence of the source. Most spatial filtering operations require a source which is a spatially coherent source with only minimal temporal coherence. Use of an interference filtered arc lamp or a GaAs laser would retain sufficient spatial coherence while reducing the coherence lengths so that the first and second order reflections would not interfere. Finally, if the $\text{Bi}_{12}\text{SiO}_{20}$ crystal has sufficient wedge between front and back surfaces, the fringes will become high enough frequency either to be ignored or to be eliminated by blocking the second reflected order with an off-axis stop in the Fourier plane.

Figure 6-4 is a magnified photograph of the Fraunhofer diffraction spectrum of the PROM crossed grating image. The irregular shape of the diffraction orders is due to a lack of flatness in the faces of the $\text{Bi}_{12}\text{SiO}_{20}$ crystals. The crystals were polished to a flatness of only approximately 3 to 5 waves rms with coarse microstructure. Since completion of the NASA contract continued studies of crystal polishing techniques have been supported by Itek. Recent polishing has produced $\text{Bi}_{12}\text{SiO}_{20}$ chips having flatness to better than 1/2 wave rms, with a commensurate reduction in micro-roughness. Continued improvement is expected,

with the eventual goal of producing chips having flatness of better than 1/5 wave rms.

When a slit filter is inserted in the Fourier plane which allows only the central, vertical row of orders to pass, the reconstructed image is shown in Figure 6-5. The vertical grid lines have been eliminated and only the horizontal lines are reconstructed. There is some reduction in sharpness of the lines in the reconstruction. Due to their irregularity, the slit has blocked some of the light from the diffraction order which was passed, causing the image blurriness.

The importance of this experiment is that it demonstrates the incoherent-to-coherent conversion capability of the optical-to-optical interface device. An incoherent image was written on the device and read out with coherent light. Fourier analysis was performed on the image, or demonstrated by the Fraunhofer spectrum. Fourier synthesis operations were also performed on the image demonstrated by the filtering and reconstruction operations.

6.4 Converter Operational Characteristics -

In addition to the imaging and optical Fourier transformation of a range of reflective and transmissive targets, the following characteristics were demonstrated for the delivered noncoherent-to-coherent converters.

1) Image generation time - The device was cyclically operated at a rate of 10 Hz. Each complete cycle consisted of a priming step which completely erased the old image and prepolarized (primed) the electro-optic crystal for a new write-in; exposure into the converter of a new noncoherently illuminated image; and readout of the image with red coherent light (632.8nm).

2) Noncoherent-to-coherent conversion - This was demonstrated by writing in with noncoherent mercury light and reading out with coherent laser light. The readout image was demonstrated to show optical Fourier transformation and, after spatial filtering, Fourier synthesis in a reconstructed image.

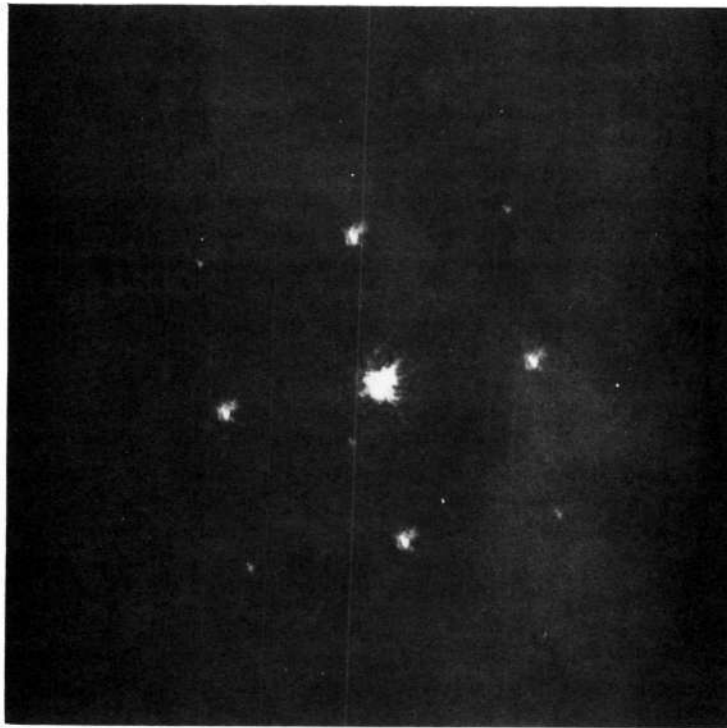


Fig. 6-4 Power spectra of 10 lp/mm (grating as seen in Fourier plane)

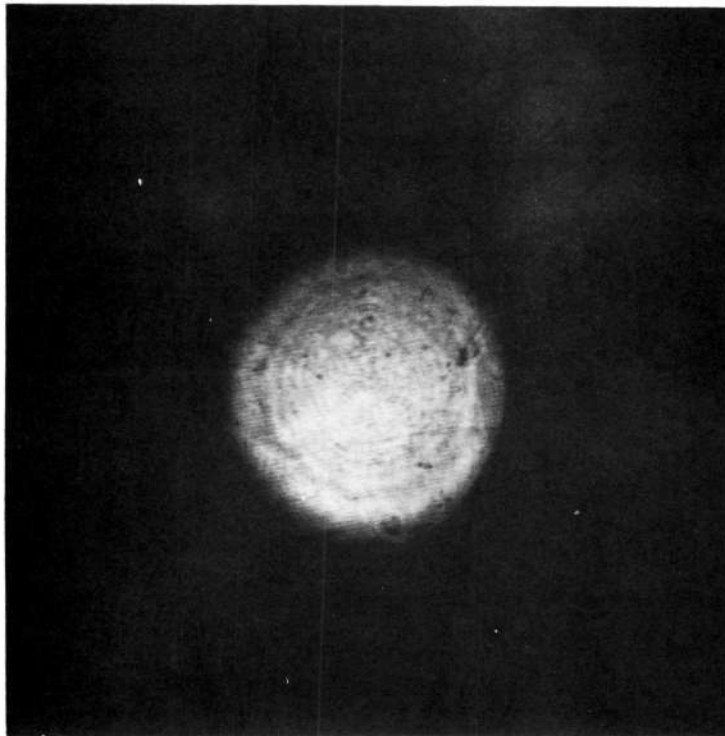


Fig. 6-5 Grating with one set of lines removed by inserting slit filter in Fourier plane located between OID and output plane

3) Optical transfer efficiency (the inverse ratio of the intensity of the readout light before entering the converter to the intensity output from the device with 1/2 wave electro-optic voltage applied) - The optical efficiency of the delivered devices was greater than 8%. The attenuation factors were the losses at the partially transparent front Pt electrode (35% reflecting) and the losses at the dichroic reflector (80% reflecting). Reflections at the other optical interfaces and crystal absorption accounted for the other losses.

4) Readout contrast - Between the fully exposed and unexposed regions of the converter the contrast ratio was demonstrated to be in excess of 50 to 1 both for reflective and transmissive write-in. The contributing factors in reducing image contrast were strain in the crystal (which adds a background electro-optic bias level) and steady state readout while the device is recycling (see explanation below).

The delivered devices which showed considerable strain bias were 900 micrometers thick. Devices fabricated at Itek since the end of the contract, which were made only 250 micrometers thick, have shown dramatic reduction in strain and yielded contrast ratios approaching 5000 to 1.

Since readout was monitored continuously including the erase/prime period, the contrast was therefore averaged over a full cycle. Sampling the readout between erase/prime/write-in periods (see Fig. 2-5) yields nearly a factor of 2 increase in contrast.

5) Size - the useful working image areas of the two delivered devices were 1 cm² and 2 cm². These areas were shown to be sufficient for writing and reading 64 x 64 element checkerboard images.

6.5 Photographic Results -

A large number of reflection and transmission targets were imaged onto the converter with noncoherent light and read-out with laser light using the optical systems described in a previous section. Polaroid photographs were taken of the reconstructed images

and Fraunhofer diffraction (Fourier transform) patterns from the converter images for each target, along with photos of the diffraction patterns obtained when the write-in image (photographic negative) was used as the coherent light modulator in the system. The latter are labeled "comparison Fourier transform". Magnifications and exposures were adjusted as suitable for each image. Table 6-1 lists the photographs and targets included and summarizes the exposure and magnification data. All transmission targets were imaged at a 1 to 1 magnification using 436 nm filtered light. Reproductions of the photographs described in Table 6-1 appear in Figures 6-6 through 6-12.

Photo Description (Fig. No.)

Exposure Conditions

Transmission Target 1:

Three-bar single-frequency @ three angles

- | | |
|--|---|
| 1. Reconstructed Image (6-6a) | 1/2 sec. exposure thru a 1.2 neutral density filter onto Polaroid P/N
4X enlargement |
| 2. Fourier transform (6-6b) | 1/2 sec. exposure onto Polaroid P/N
8X enlargement |
| 3. Comparison Fourier transform (6-6c) | 1 sec. exposure thru 1.2 neutral density filter onto Polaroid P/N
8X enlargement |

Transmission Target 2:

Multi-bar multi-frequency @ three angles

- | | |
|--|--|
| 4. Reconstructed image (6-7a) | 1/25 sec. exposure onto Polaroid P/N
4X enlargement |
| 5. Fourier transform (6-7b) | Same as 2 above |
| 6. Comparison Fourier transform (6-7c) | Same as 3 above |

Transmission Target 3:

Triangle

- | | |
|---|---|
| 7. Reconstructed image (6-8a) | 1/200 sec. exposure onto Polaroid P/N
4X enlargement |
| 8. Reconstructed image (6-8b) | 1/2 sec. exposure thru 1.2 neutral density filter onto Polaroid P/N
4X enlargement |
| 9. Fourier transform (6-8c) | Same as 2 above |
| 10. Comparison Fourier transform (6-8d) | Same as 3 above |

Transmission Target 4:

Checkerboard

- | | |
|--|-----------------|
| 11. Reconstructed image (10 x 10 squares) (6-9a) | Same as 1 above |
|--|-----------------|

Table 6-1 Description of Performance Test Targets
and Output Image Photographs

12. Fourier transform (64 x 64 squares) (6-9b) Same as 2 above
13. Comparison Fourier transform
(64 x 64 squares) (6-9c) Same as 3 above

Transmission Target 5:
Airstrip

14. Reconstructed image (6-10a) 1/100 sec. exposure onto Polaroid P/N
4X enlargement
15. Fourier transform (6-10b) 1/10 sec. exposure onto Polaroid P/N
8X enlargement
16. Comparison Fourier transform (6-10c) Same as 3 above

Reflection Target 1:
Checkerboard

17. Reconstructed image (6-11a) Same as 7 above
18. Fourier transform (6-11b) 1/200 sec. exposure onto Polaroid P/N
8X enlargement

Reflection Target 2:
Half Plane

19. Reconstructed image (6-12a) Same as 7 above

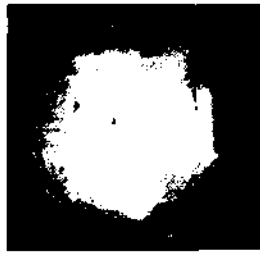
Strain pattern (no voltage applied to device)

20. Output plane image (6-12b) Same as 7 above

No input light (voltage applied to device)

21. Output plane image (6-12c) Same as 7 above

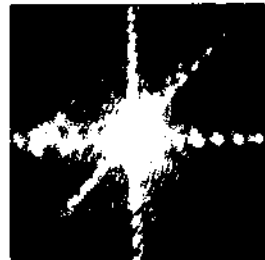
Table 6-1 Continued



a. Reconstructed image



b. Fourier transform



c. Comparison Fourier transform

Fig. 6-6 OID output images using three-bar single frequency input target



a. Reconstructed image

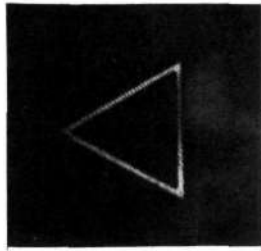


b. Fourier transform

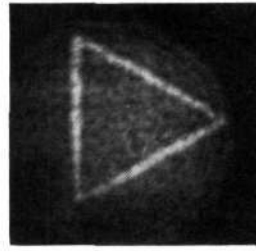


c. Comparison Fourier transform

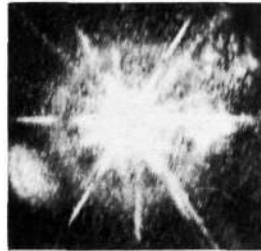
Fig. 6-7 OID output images using multi-bar multi-frequency input target



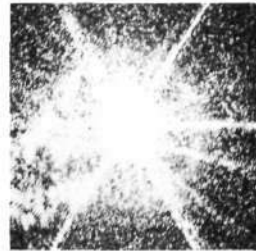
a. Reconstructed image



b. Reconstructed image

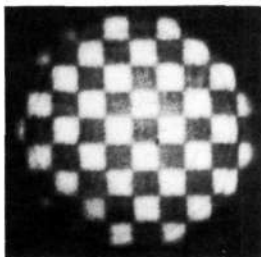


c. Fourier transform

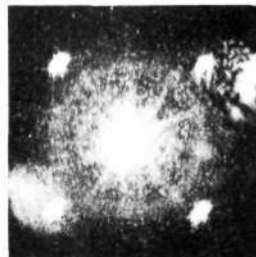


d. Comparison Fourier transform

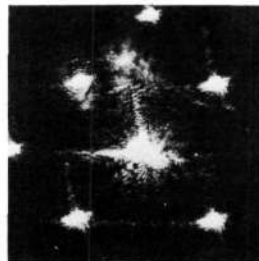
Fig. 6-8 OID output images using triangle target



a. Reconstructed image
(10 x 10 squares)

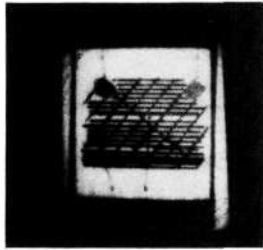


b. Fourier transform
(64 x 64 squares)



c. Comparison Fourier transform (64 x 64 squares)

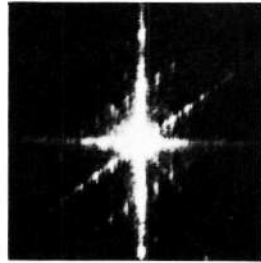
Fig. 6-9 OID output images using checkerboard target (transmitting)



a. Reconstructed image

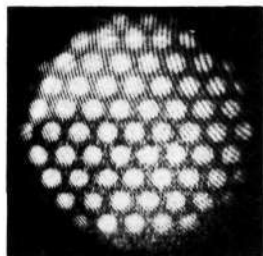


b. Fourier transform

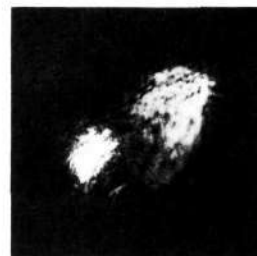


c. Comparison Fourier transform

Fig. 6-10 OID output images using airstrip target



a. Reconstructed image

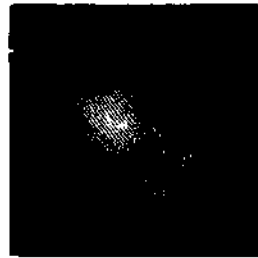


b. Fourier transform

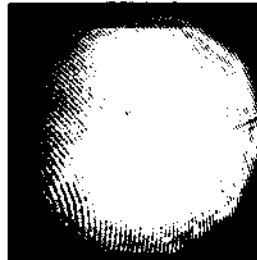
Fig. 6-11 OID output images using checkerboard target (reflecting)



a. Reconstructed image



b. Output plane image



c. Output plane image

Fig. 6-12 OID output image for low frequency target (reflecting) plus strain pattern and no signal pattern

7. PROBLEMS ENCOUNTERED

Many of the outstanding problems encountered during the course of the program have already been mentioned in previous sections; however, these problems and other problems encountered will be summarized here for the purpose of indicating the direction that future work should take (Section 9).

7.1 Crystal Cracking -

The tendency for cracking of large diameter $\text{Bi}_{12}\text{SiO}_{20}$ ingots under normal device fabrication conditions has its origin in the lattice structure of the crystal, specifically the large thermal expansion coefficient which is of the order of six times that of germanium. Other factors contributing to cracking are the large piezo-electric effect in $\text{Bi}_{12}\text{SiO}_{20}$ which strains the crystal under pulse operation and the necessity of adding the second oxide phase (SiO_2) in order to stabilize the B.C. cubic structure. This oxide is known to change the lattice constant.

7.2 Birefringent Strain -

The strains which in the limit produced cracking as discussed above also induced birefringence into a normally isotropic crystal. When viewed through crossed analyzers, as in the readout process, this birefringence showed up as a background illumination in the readout display (see Fig. 6-12b).

7.3 Contrast Ratio -

Loss of contrast is primarily due to unwanted light in the "dark" regions of the display. One source of this illumination is birefringent strain as mentioned above. A second is scattered light from various interface surfaces in the device and on other optical components. Since this scattered light is primarily unpolarized approximately one-half of it will pass through the readout analyzer. Another contributor to loss of contrast is the transient light pulse which occurs during the erase/prime step (see Figure 2-5 and the first term of equation 2). The one remaining factor which determines contrast is the intensity of write-in illumination and the

sensitivity of the device to this radiation. The decay time constant, τ_2 , in equation 2 is inversely related to input illumination and device sensitivity and an unwanted increase in τ_2 results in an increase in "dark" region illumination.

The loss of contrast due to the transient light pulses mentioned above is demonstrated clearly in Figures 6-8a and 6-8b. In Figure 6-8b a neutral density filter was used to reduce the intensity of the readout light. This allowed an increase in photographic exposure time to give a time averaging over several converter cycles. In Figure 6-8a the photo was taken without a neutral density filter at a 5 millisecond exposure time, which is considerably less than the converter cycle time. The correct timing of the exposure cycle was found by trial and error and considerable enhancement of the image contrast is observed.

7.4 Sensitivity -

The coherent image contrast ratio for reflection targets (Figure 6-11a) was found to be considerably less than for transmission targets (Figure 6-9a). This is believed to be due to the relative insensitivity of the converter to tungsten illumination (3400°K).

7.5 Strain -

The effect of strain in reducing contrast is depicted in Figure 6-12b. Since no voltage was applied to the device during this photograph a dark field should have appeared in the coherent output image plane. Instead a low frequency patch of illumination is present. This is believed to be due to birefringence induced into the $\text{Bi}_{12}\text{SiO}_{20}$ crystal by strain.

7.6 Reflections and Coherent Interference Patterns -

A degrading effect on the coherent output image quality was the "finger print" effect clearly depicted in Figure 6-12c. This image ideally should show a uniform bright field due to the absence of write-in light. The pattern depicted in Figure 6-12c is believed due to an interference pattern caused by reflections either internal or external to the device.

The reflecting interfaces to be considered are the platinum electrodes and the dichroic layer which have reflectivities of 35% and 80% respectively. It is believed that the initial front surface reflection of readout light (35%) would be blocked by the crossed analyzer. However, an internal reflection occurs at this electrode interface when the transmitted beam exits the converter after a roundtrip through the $\text{Bi}_{12}\text{SiO}_{20}$ crystal. This creates a secondary beam which also undergoes electro-optic phase modulation (twice) as a result of a second round trip through the $\text{Bi}_{12}\text{SiO}_{20}$ crystal. The primary and secondary beams, differing in intensity by approximately 30% and having a relative phase relationship dictated by the birefringence in the crystal could interfere to form the observed pattern of Figure 6-1c.

8. PROJECT RESULTS

Two incoherent-to-coherent converters were designed, built, tested, and delivered to NASA Goddard during the course of this work as described in the previous sections. These converters performed in accordance with the work statement and Figures 6-6 through 6-11 give photographic evidence of the ability of these devices to perform an incoherent-to-coherent conversion with an optical quality suitable for Fourier transforming the converted image.

9. RECOMMENDATIONS

A four year R & D effort in light sensitive electro-optic crystals at Itek has resulted in the development of a device which has considerable potential for many optical processing applications. With NASA's support under NAS 5-11486 a feasibility model of an optical-to-optical interface device was constructed. Although the device operation is generally within our expectations and the design goals of the contract, we believe that the possibility for improved performance as well as increased operational versatility (the development of a universal optical processing element) exists.

To achieve these aims it is proposed to combine our light sensitive electro-optic element with an image intensifier. A unique optical processing device results (Figure 9-1). The photocathode, of course, will provide greatly enhanced sensitivity over the entire visible spectrum (desirable for the ultimate optical-to-optical converter). The structure itself is basically an optical converter with built-in image storage. It can be operated either in a READ while WRITE or WRITE, STORE, and READ mode. Furthermore if two images are stored in the device in sequence the resulting output image will be an inverted OR (i.e. NOR) relationship between the two input images. Several of these universal logic elements can be combined to perform desired AND, OR logic comparisons between optical images in parallel.

In addition to the performance advantages afforded by the intensifier/ electro-optic crystal combination in terms of spectral sensitivity and logical flexibility the structure should have improved optical quality afforded by sandwiching the crystal between optical flats with the aid of index matching fluid. Furthermore the low reflection losses of semiconductor electrodes should minimize unwanted interference patterns caused by interface reflections.

Although an improved converter structure is proposed above work with existing devices should be performed so that they may be fully characterized as to photosensitivity, undesirable optical effects (such as fringing, birefringent strain and multiple internal reflections), stability of operation, contrast ratio, response time, storage time, and resolution. Then guides for directing further materials and device improvement investigations can be formulated.

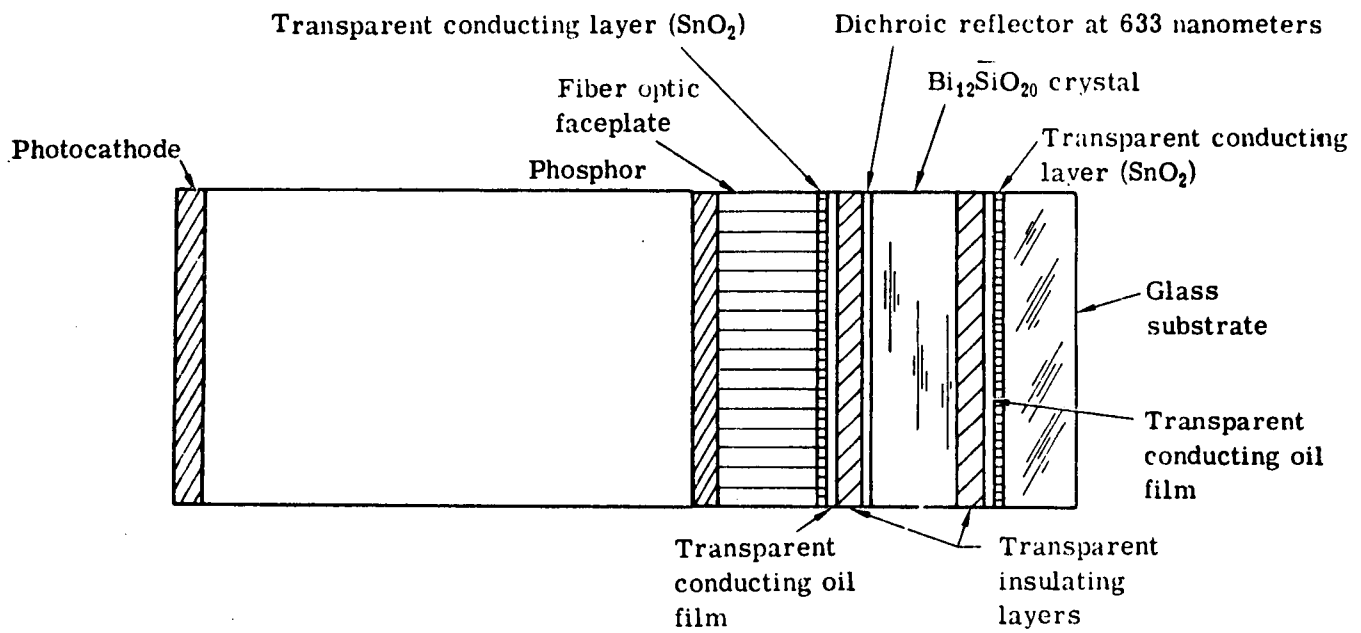


Fig. 9-1 Proposed incoherent to coherent image converter tube

10. NEW TECHNOLOGY

No new technology was developed during the course of this contract.

11. APPENDIX

11.1 Diffraction Efficiency Calculations

Analysis of the operation of the PROM for the coherent readout mode after exposure with a sinusoidal intensity demonstrates that the operation of the modulator is similar to a phase grating.

When the polarized light making a 45-degree angle with the crystal's birefringent axes passes through the modulator, the local ordinary and extraordinary disturbances are advanced or retarded respectively by a phase shaft, Φ . If the exposing intensity pattern is sinusoidal, varying only in the x direction, then the problem need only be treated in one dimension. If the phase shift is proportional to the exposing intensity distribution, then Φ can be written in the form

$$\Phi = \frac{\Phi_A}{1+m}(1 + m \cos \omega_o X)$$

Here Φ_A is the device's maximum phase shift at the half-wave voltage, m is the modulation, and ω_o is the spatial frequency of the sinusoidal exposure pattern.

The complex amplitude distribution after modulation by the device has two components, A and B where

$$A = \frac{E}{\sqrt{2}} \exp(-i\Phi) = \frac{E}{\sqrt{2}} \exp\left[-i\frac{\Phi_A}{1+m}(1 + m \cos \omega_o X)\right]$$

$$B = \frac{E}{\sqrt{2}} \exp(+i\Phi) = \frac{E}{\sqrt{2}} \exp\left[+i\frac{\Phi_A}{1+m}(1 + m \cos \omega_o X)\right]$$

where E is the amplitude of the incident wave.

A and B are in spatial quadrature, so their intensities not their complex amplitudes add. The intensity spectrum is obtained by expanding A and B in a Bessel series, Fourier transforming, and adding the square moduli of their resulting complex amplitudes. Therefore, the zero and positive or negative first orders of the intensity spectrum, I_S , with no analyzer introduced in the readout beam, has the form

$$I_S = E^2 J_0^2 \left(\frac{m\Phi_A}{1+m} \right) \delta(o) + E^2 J_1^2 \left(\frac{m\Phi_A}{1+m} \right) \delta(\pm\omega_0 X)$$

where J_0 and J_1 are the zero- and the first-order Bessel functions of the first kind and δ is the Dirac delta function.

When an analyzer is inserted between the PROM and the frequency plane with its axis of polarization rotated 90 degrees with respect to the polarization of the incident readout beam, the complex amplitude, C, immediately after the analyzer is

$$C = \frac{E}{2} \left\{ \exp \left[+ \frac{i\Phi_A}{1+m} (1 + m \cos \omega_0 X) \right] - \exp \left[- \frac{i\Phi_A}{1+m} (1 + m \cos \omega_0 X) \right] \right\}$$

Again rearranging terms, expanding in a Bessel series, Fourier transforming, and calculating the intensity spectrum, I_C , gives

$$I_C = E^2 \sin^2 \left(\frac{\Phi_A}{1+m} \right) J_0^2 \left(\frac{m\Phi_A}{1+m} \right) \delta(o) + E^2 \cos^2 \left(\frac{\Phi_A}{1+m} \right) J_1^2 \left(\frac{m\Phi_A}{1+m} \right) \delta(\pm\omega_0 X)$$

And, finally, if the analyzer is parallel to the direction of polarization, the amplitude after the analyzer, P, is

$$P = \frac{E}{2} \left(\exp \left\{ \frac{i\Phi_A}{1+m} [1 + m \cos (\omega_0 X)] \right\} + \exp \left\{ - \frac{i\Phi_A}{1+m} [1 + m \cos (\omega_0 X)] \right\} \right)$$

The intensity spectrum, I_p , is calculated as

$$I_p = E^2 \cos^2 \left(\frac{\Phi_A}{1+m} \right) J_0^2 \left(\frac{m\Phi_A}{1+m} \right) \delta(o) + E^2 \sin^2 \left(\frac{\Phi_A}{1+m} \right) J_1^2 \left(\frac{m\Phi_A}{1+m} \right) \delta(\pm\omega_0 X)$$

Figs. A-1 through A-5 are examples of the percent diffraction efficiency of the first-order intensity spectra plotted against effective modulation on the device, after the effect of the MTF, for likely values of Φ_A , E is taken as 1.0 and losses due to reflections from the optical surfaces and absorption are assumed to be negligible. Figure A-1 shows results from the crossed analyzer for values of Φ_A ranging from $\pi/2$ to $\pi/6$. Figs. A-2, A-3 and A-4 compare results for operation with no analyzer, parallel analyzer, and crossed analyzer for typical values of Φ_A ($\pi/2$, $\pi/3$, and $\pi/4$, respectively). These results demonstrate that unless the device operates near the practical maximum phase shift of $\pi/2$, the crossed analyzer mode is more efficient than the parallel analyzer. While the "no analyzer" mode is always more efficient than the crossed analyzer mode, the crossed polarizer reduces the background noise, front surface reflections, and zero-order components, so the small gain in diffraction efficiency is traded for considerable improvement in signal to noise ratio.

Fig. A-5, which plots diffraction efficiency against Φ_A ($m=1.0$), shows that efficiencies of over 30 percent are possible if Φ_A is close to π . This will require voltage of over 4,000 volts across the crystal.

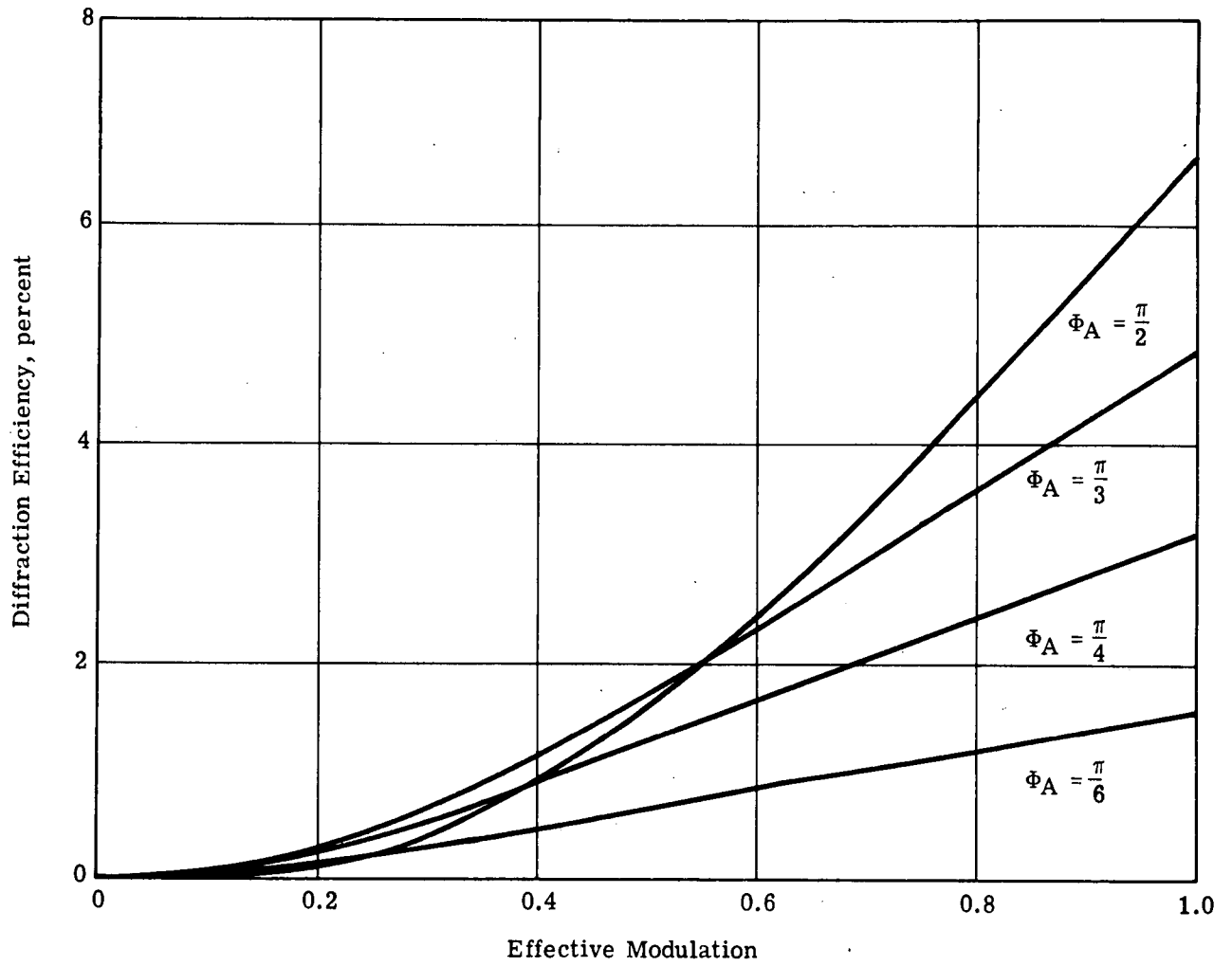


Fig. A-1 First-order diffraction efficiency (crossed analyzer)

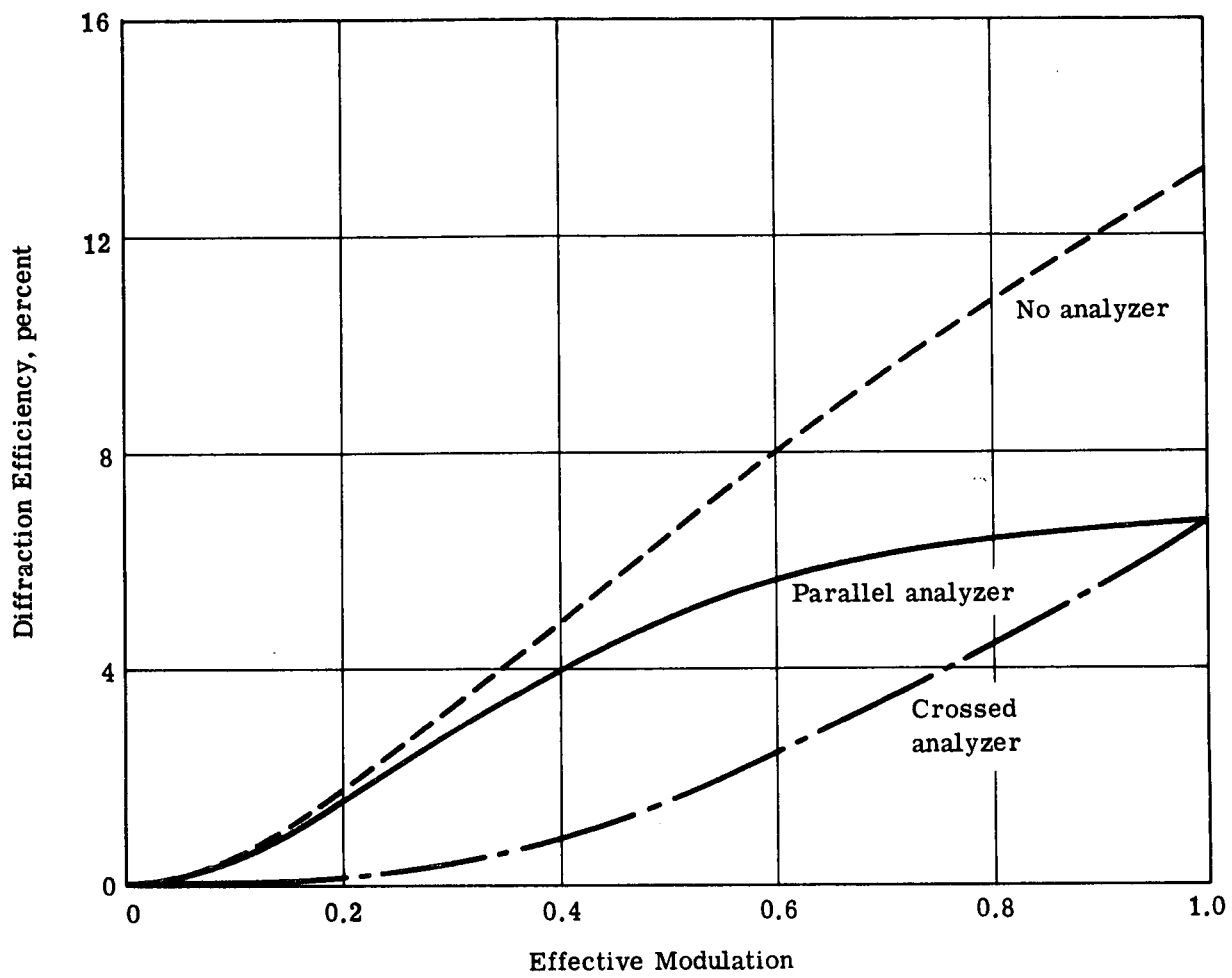


Fig. A-2 First-order diffraction efficiency ($\Phi_A = \pi/2$)

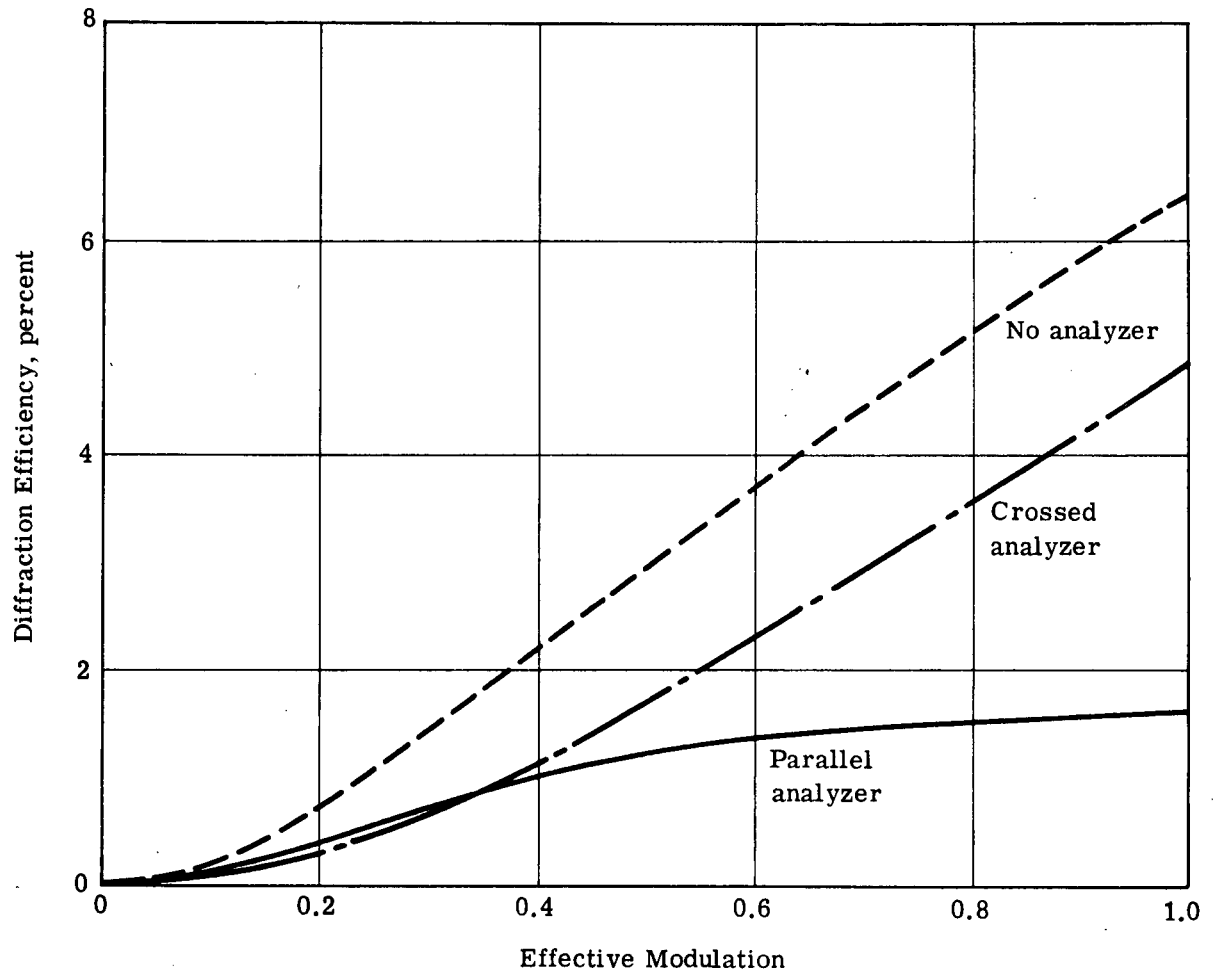


Fig. A-3 First-order diffraction efficiency ($\Phi_A = \pi/3$)

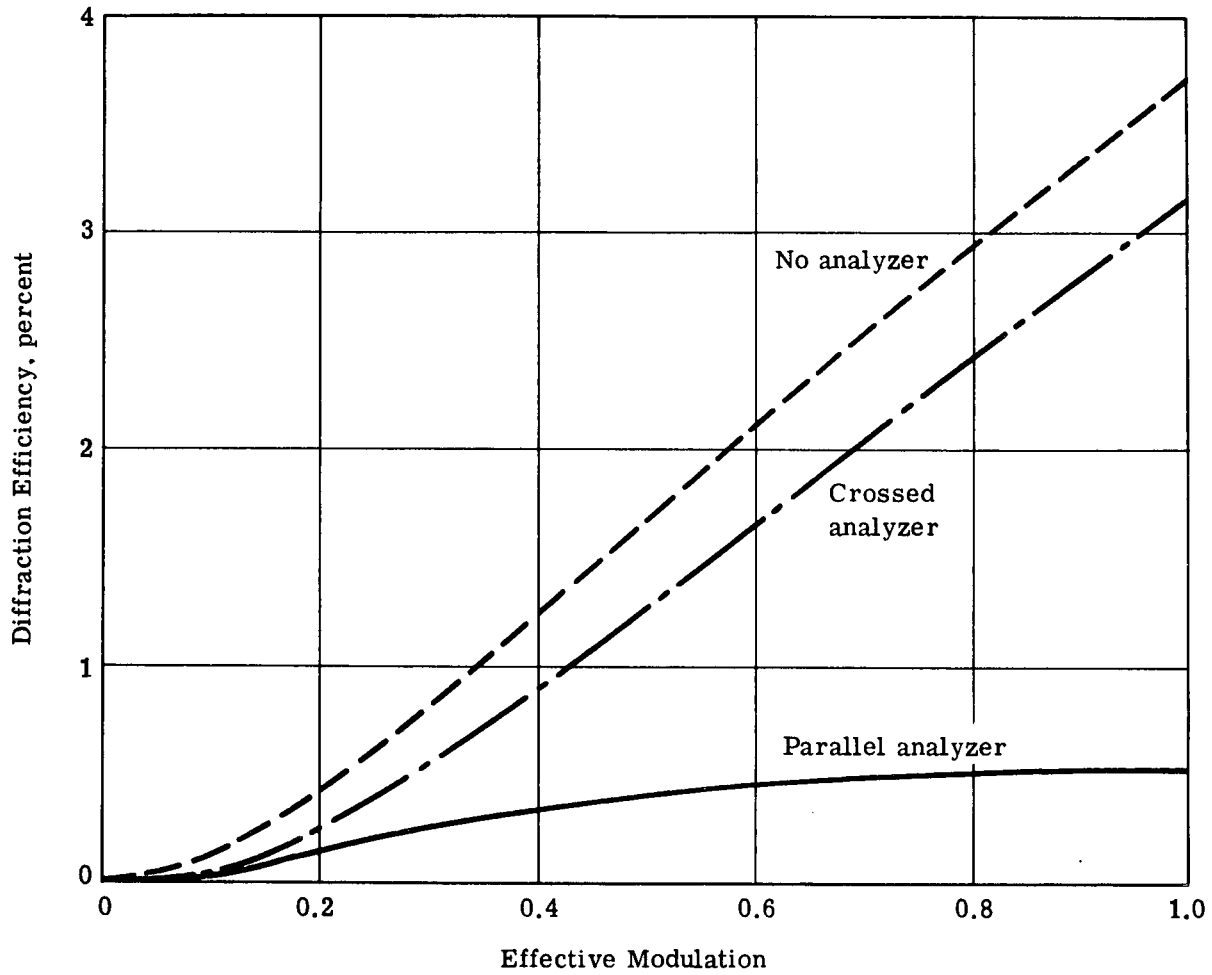


Fig. A-4 First-order diffraction efficiency ($\Phi_A = \pi/4$)

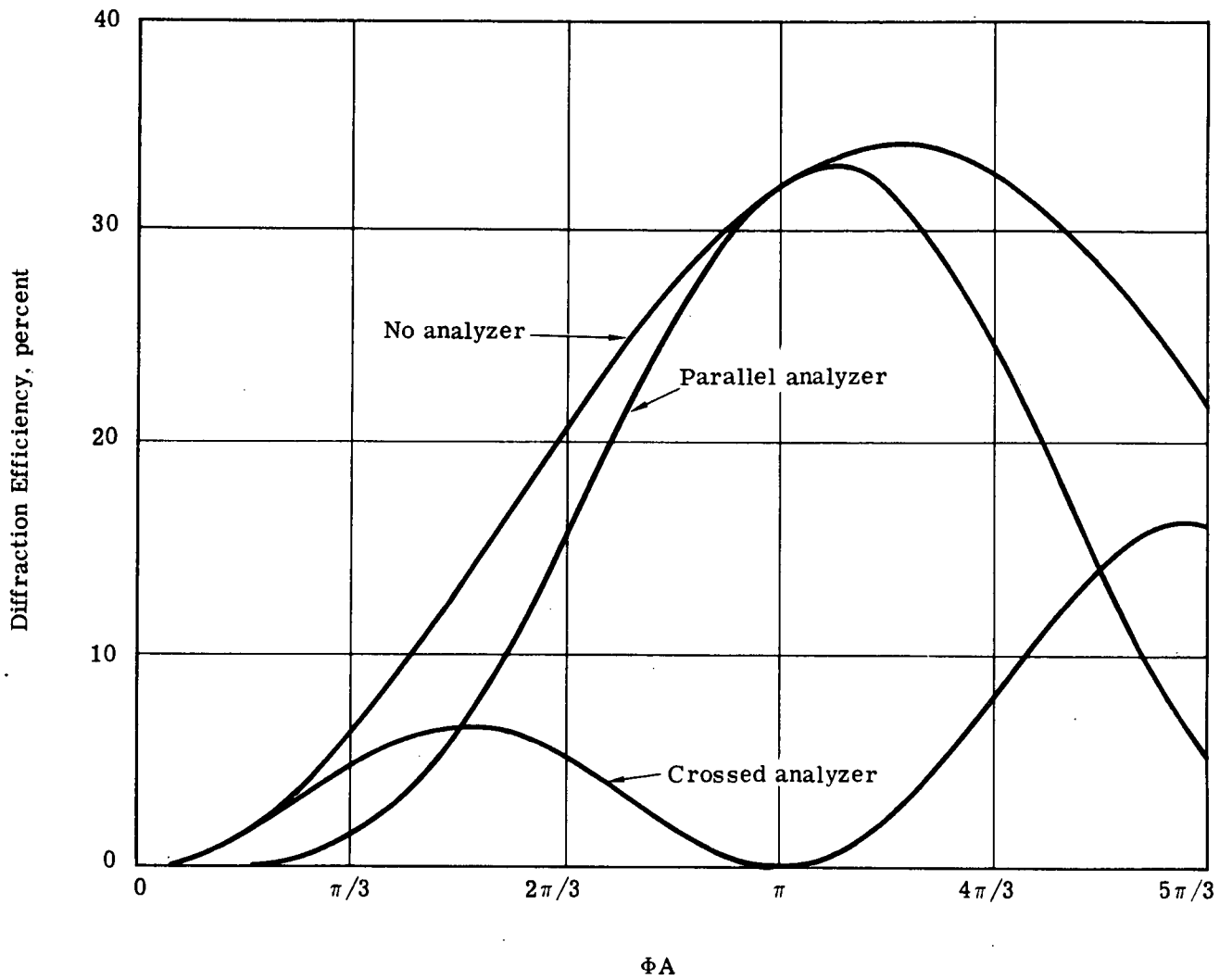


Fig. A-5 First-order diffraction efficiency ($m=1$)

11.2 Quantum Efficiency Calculation

A 0.013 inch thick PROM having total Parylene thickness (sum of two layers) of 5 micrometers was evaluated for sensitivity to 4358 Å radiation. The device was primed by applying 1200 volts and uniform illumination. This charged the Parylene layers up to 1200 volts (600 volts across each layer) in the manner depicted in Figure 2-3a and 2-3b. The device was then shorted (see Fig. 2-3c) and the 4358 Å write-in radiation was applied (see Fig. 2-3d). It was observed that an exposing write-in intensity of 275 micro-watts/cm² caused the readout light (observed through a crossed analyzer) to drop to the e⁻¹ point in 10 milliseconds.

Since the readout light intensity is roughly proportional to the square of the voltage across the Bi₁₂SiO₂₀ which is in turn proportional to the stored charge it follows that when the readout light intensity has been reduced to the e⁻¹ point the device has roughly discharged to the e^{-0.5} point. Therefore the change in stored charge is $1 - e^{-0.5} = 0.39$ of the original stored charge. This change in charge can be computed by first calculating the charge stored across the Parylene layers as follows:

$$Q = (\epsilon \epsilon_0 V)/t,$$

where ϵ = Parylene dielectric constant = 2.6

ϵ_0 = dielectric constant of air = 8.85×10^{-14} farad/cm

V = applied voltage = 1200 volts

t = parylene thickness = 5 micrometers

substituting,

$$Q = 1200 \times 2.6 \times 8.85 \times 10^{-14} \times (5 \times 10^{-4})^{-1} = 5.5 \times 10^{-7} \text{ coul/cm}^2.$$

Therefore the change in charge due to write-in exposure is

$$0.39 Q = 2.2 \times 10^{-7} \text{ coul/cm}^2 = 1.3 \times 10^{12} \text{ electrons/cm}^2.$$

The exposing radiation which produced this discharge was 275 micro-watts/cm² for 10 milliseconds or 2.75 microjoule/cm². This can be converted to photons/cm² by remembering that each photon of radiation at 4358 Å contains 2.9 ev of energy. Therefore

$$2.75 \text{ microjoule/cm}^2 = 1.72 \times 10^{13} \text{ ev/cm}^2 = 6 \times 10^{12} \text{ photons/cm}^2.$$

Therefore, the quantum efficiency, defined as the ratio of electrons discharged per incident photon becomes:

$$Q. E. = 100 \times (1.3/6) = 22\%$$

12. REFERENCES

- (1) D. S. Oliver et al., Appl. Phys. Lett. 17, 416 (15 November 1970).
- (2) D. S. Oliver and W. R. Buchan, IEEE Trans. Electron Devices ED-18 (September 1971).
- (3) S. L. Hou and D. S. Oliver, Appl. Phys. Lett. 18, 325 (15 April 1971).
- (4) M. Behrndt and S. Moreno, J. Vac. Sci. Technol. 8, 494 (1971).
- (5) P. Vohl et al., J. Electrochem. Soc. 118, 1842 (1971).
- (6) R. Aldrich et al., J. Appl. Phys. 42, 493 (1971).
- (7) P. Vohl, Mat. Res. Bull. 4, 689 (1969).
- (8) F. G. Wakim, J. Appl. Phys. 41, 835 (1970).
- (9) J. Genthe and R. Aldrich, Thin Solid Films, 8, 149 (1971).
- (10) A. A. Ballman, J. Crystal Growth 1, 37-40 (1967).